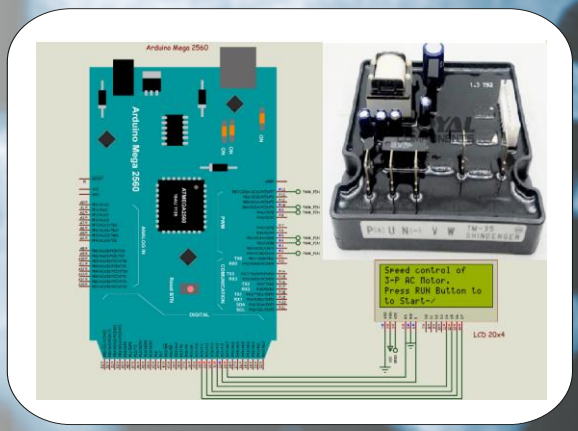
International journal
for science, technics and
innovations for the industry

MACHINES TECHNOLOGIES MATERIALS

YEAR XIV Issue 6 / 2020 ISSN PRINT 1313-0226
ISSN WEB 1314-507X



Published by
Scientific technical
Union of Mechanical Engineering

MACHINES. TECHNOLOGIES. MATERIALS

INTERNATIONAL SCIENTIFIC JOURNAL

ISSN PRINT 1313-0226, ISSN WEB 1314-507X, YEAR XIV, ISSUE 6 / 2020

INTERNATIONAL EDITORAL BORARD

EDITOR IN CHIEF:		
Georgi Popov	Technical University of Sofia	BG
MEMBERS:		
Abdrakhman Naizabekov	Rudny industrial institute	KZ
Ahmet H. Ertas	Bursa Technical University	TR
Albert Albers	Karlsruhe Institut of Technology	DE
Andrzej Golabczak	Lodz University of Technology	PL
Andrzej Huczko	Warsaw University	PL
Dimitar Karaivanov	University of Chemical Technology and Metallurgy, Sofia	BG
Emilia Abadjieva	Akita University	JP
Erdem Camurlu	Akdeniz University, Antalya	TR
Eugen Sheregii	University of Rzeszow	PL
Franz Haas	Graz University of Technology	AT
Galina Nicolcheva	Technical University of Sofia	BG
Gennadii Bagliuk	Institute for Problems of Materials Science NAS of Ukraine, Kiev	UA
Georgii Raab	Ufa State Aviation Technical University	RU
Gregory Gurevich	Shamoon College of Engeeniring, Ashdod	IL
Hiroyuki Moriyama	Tokai University, Hiratsuka	JP
Idilia Batchkova	University of Chemical Technology and Metallurgy, Sofia	BG
Ivan Kralov	Technical University of Sofia	BG
Ivan Kuric	University of Zilina	SK
Julieta Kaleicheva	Technical University of Sofia	BG
Katia Vutova	Institute of Electronics, Bulgarian Academy of Sciences	BG
Maria Nikolova	Angel Kanchev University of Ruse	BG
Natasa Naprstkova	Jan Evangelista Purkyne University in Usti nad Labem	CZ
Oana Dodun	Gheorghe Asachi Technical University of Iasi	RO
Ognyan Andreev	Technical University of Sofia	BG
Predrag Dasic	High Technical Mechanical School of Trstenik	RS
Rasa Kandrotaite	Kaunas University of Technology	LT
Raul Turmanidze	Georgian Technical University, Tbilisi	GE
Roumen Petrov	Ghent University	BE
Sergey Dobatkin	National University of Science and Technology "MISIS", Moscow	RU
Souren Mitra	Jadavpur University, Kolkata	IN
Svetlana Gubenko	National Metallurgical Academy of Ukraine, Dnipro	UA
Vedran Mrzljak	University of Rijeka	HR
Wu Kaiming	Wuhan University of Science and Technology	CN

TECHNICAL EDITORS:
M. Sc. Eng Radoslav Daskalov, M. Sc. Eng Oleg Mihailov

Scientific and technical union of mechanical engineering
108 R. S. Rakovski str., Sofia, Bulgaria
www.stumejournals.com, office@stumejournals.com

C O N T E N T S

MACHINES

Evolution of rolling bearing life rating through the standardization
Tatjana Lazović, Ivana Topalović 222

3-phase motor speed regulator based on microcontroller and intelligent power driver controller
Stefanov G., Cekerovski T., Citcuseva Dimitrova B., Stefanova S. 226

TECHNOLOGIES

Evolution of creative thought with elements of artificial intelligence on example of synthesis of clamping mechanisms
Kuznetsov Yuri 230

Stress-strain state of workpiece from Cu-Cr alloy processed by severe plastic deformation by ECAP
Asfandiyarov Rashid, Aksenov Denis, Dr. Eng. Raab Georgy 237

Remote real-time control of autoclave sterilization process
Stoyanka Madzharova, Rosen Gerasimov, Adriana Prodanova , Hristo Dinkov 240

Model for high-pressure water atomization of metal melt using a vortex type jet
Ternovoy Yu., Bagliuk G., Panova V. 243

MATERIALS

Structure and properties of microarc oxide coatings on high-temperature aluminum alloy
Valeriia Subbotina, Oleg Sobol' 247

Layered composites based on niobium with silicide-carbide or silicide-boride hardening
Korzhov Valery Polikarpovich, Kiiko Vyacheslav Mikhailovich, Prokhorov Dmitry Vladimirovich,
Zheltyakova Irina Sergeevna 251

Hydrophilized unsaturated polyester resin based on a two-component system of sulfur and cement
Cherkezova R., Hristova T. Zafirova K. 255

Evolution of rolling bearing life rating through the standardization

Tatjana Lazović[1], Ivana Topalović[2]
University of Belgrade, Faculty of Mechanical Engineering[1], Belgrade, Serbia
Institut for Standardization of Serbia[2], Belgrade, Serbia
tlazovic@mas.bg.ac.rs

Abstract: *The operational ability of a rolling bearing selected for a specific application is assessed based on service life. The basic formula for bearing rating life was established more than 70 years ago by A. Palmgren. The first standard presenting a basic mathematical model for rating life calculation was published in 1962 (ISO/R281). The content of this standard has been revised and the next version was published in 1977 (ISO 281-1). The novelty was the introduction of adjustment factors for reliability other than 90%. This standard was replaced by the ISO 281 standard in 1990, which introduced additional adjustment factors for special bearing properties and operating conditions. The latest version of the ISO 281 standard was published in 2007. This standard provides a procedure for calculating the modified service life by taking into account the additional impacts of lubrication condition, lubricant contamination and limit fatigue load. Furthermore, the document ISO/TS 16281 was published in 2008 introducing the influence of bearing internal clearance and misalignment in the rating life calculation. An overview of the development of a standardized formula for bearing rating life is given in this paper, on the example of deep groove ball bearing under radial operational loading.*

Keywords*: ROLLING BEARINGS, RATING LIFE, ADJUSTED RATING LIFE, MODIFIED RATING LIFE, STANDARDIZATION, ISO*

1. Introduction

A first discussion on the international level on standardization of the calculation method for load ratings of rolling bearings took place at the conference of the International Federation of the National Standardizing Associations (ISA) held in 1934 [1,2]. The first proposals for the definition of the fundamental concept to load rating and life calculation standards were included in the ISA 1945 report on the state of rolling bearing standardization. This report was distributed in 1949 as a document of Technical Committee ISO/TC 4 and the definitions it contained are in essence those given in ISO 281:2007 [3], which is the last version of the standard on the bearing life and basic dynamic load rating concepts. These concepts are based on the theory of Palmgren and Lundberg, using Weibul statistics [4-6]. The first proposal to ISO named "Load rating of ball bearings" was presented in 1950. After that, load rating and life calculation methods were studied by ISO Technical committee 4 at eleven meetings from 1951 to 1959. Finally, The draft ISO Recommendation was issued in 1959, and ISO/R281 was accepted by ISO Council in 1962 [1,2].

In 1964, the member body from Sweden suggested that ISO/R281 has to be reviewed and submitted proposal considering the development of imposed bearing steels, which was not accepted from the technical committee. Three years later, the technical committee accepted a suggestion by the member body from Japan to do a revision of ISO/R281. The member body from the USA submitted the Draft AFMBA (Anti-Friction Bearing Manufacturers Association) standard "Load ratings and fatigue life for ball bearings" for consideration in 1970 and "Load ratings and fatigue life for roller bearings" in 1971. These proposals were investigated in detail at five meetings from 1971 to 1974 [1,2]. The third and the final Draft proposal was circulated as a Draft International Standard in 1976 and became ISO 281-1:1977. The major part of it was almost the same as ISO/R281, but, based on American investigations during the '60s, a new clause was added, dealing with adjustment of rating lifer for reliability other than 90% and for material and operating conditions [1,2]. Furthermore, supplementary theoretical background with a derivation of mathematical expressions and new factors given in ISO 281-1:1977 was published first as ISO 281-2 "Explanatory notes" in 1979 and later as ISO/TR 8646:1985 [1].

The International Standard ISO 281:1990 [7] specifies methods of calculating the basic dynamic load rating of rolling bearings manufactured from contemporary, commonly used, good quality hardened steel in accordance with good manufacturing practice and basically of conventional design, which life is associated with 90% reliability. In addition, this version of standard ISO 281 specifies calculation adjusted rating life for various reliabilities, special bearing properties and specific operating conditions. These influences are taken into account by life adjustment factors. Detailed background information regarding the derivation of formulae and factors given for this standard are found in ISO/TR 8646 [1], as it was used for the previous version as well. The Technical Specification ISO/TS 16799 published in 1999 [8] introducing different factors in the calculation of basic dynamic load ratings and equivalent load for radial and thrust angular-contact ball bearings.

ISO 281:2007 [3] specifies methods for calculating the basic rating life, which is the life associated with 90% reliability, with commonly used high quality material, good manufacturing quality and with conventional operating conditions. In addition, it gives calculating procedure for modified rating life, for reliabilities other than 90%, specific lubrication conditions, lubricant contamination, as well as fatigue load limit of the bearing raceways. Background information regarding the derivation of equations and factors in this standard is given in two technical specifications ISO/TS 1281-1 [1] and ISO/TS 1281-2 [9] published in 2008. The first edition of ISO/TR 1281-1 "Explanatory notes – Basic dynamic load rating and basic rating life" cancels and replaces the first edition of ISO/TR 8646:1985, which has been technically revised. The first edition of ISO/TR 1281-2 "Explanatory notes – Modified rating life calculation, based on a system approach to fatigue stresses" gives background information regarding the derivation life modification factors. Calculation method given in ISO 281:2007 does not consider the influence of tilted or misaligned rings and bearing clearance on the service life. The Technical Specification ISO/TS 16281:2008 describes and advanced calculation method, which considers tilting or misalignment, operating clearance and internal load distribution between rolling elements [10], but only as information for computer calculation. There is no completed a mathematical model for any modification factor to be used in life prediction calculation method. For example, the factor of the influence of internal radial clearance in radially loaded ball bearing would have values 0.3…1.0 depending on load and clearance, as it is shown in [11]. Surely, revisions of ISO standard for dynamic load ratings and rating life will be required from time to time, as the result of new scientific developments or newly obtained information concerning specific bearing types and materials [3].

An overview of ISO 281 standards for rolling bearings dynamic load rating and rating life with appropriate explanatory notes in the form of additional technical specifications to which the standards refer is made in this paper. The standard procedure for calculating the basic service life [7,3], adjusted service life [7] and modified service life [3] is presented, taking into account the influence of reliability, lubrication, contamination and fatigue load limit. A numerical example was made for the purpose of comparative analysis of the standardized calculation and the calculation using the data of the rolling bearings manufacturers.

2. ISO 281:1990

2.1. Basic rating life

The basic rating life of radial deep groove ball bearing is given by

$$L_{10} = \left(\frac{C_r}{P_r} \right)^3, \quad (1)$$

where C_r is basic dynamic radial load rating, P_r – dynamic equivalent radial load.

Subscript "10" is the probability of failure (in %) and gives information on reliability. The standard basic life formula is derived under the assumption of 90% reliability, which means that for a group of apparently identical rolling bearings, operating under the same conditions, 90% of the group is expected to attain or exceed a specified service life.

The basic dynamic radial load rating for radial contact ball bearings is given by:

$$C_r = b_m f_c Z^{2/3} D_w^{1,8}, \quad (2)$$

where b_m is the rating factor for contemporary, normally used material and manufacturing quality, depending on bearing type and design, f_c – the factor which depends on the geometry of the bearing components, the accuracy to which the various components are made, and the material, Z - number of balls, D_w – ball diameter.

Values of rating factor b_m are table data [7] and for radial deep groove ball bearings b_m=1,3. Values of f_c factor are also given in appropriate standard table [7] for different bearing types and ratio D_w/D_{pw}, where D_{pw} is pitch diameter of ball set. Instead, the mean bearing diameter $0.5(d + D)$ can also be used, where d is bearing bore diameter and D is bearing outside diameter.

Dynamic equivalent radial load P_r for radial contact ball bearing, under constant radial and axial loads is given by

$$P_r = XF_r + YF_a, \quad (3)$$

where X and Y are dynamic factors, radial and axial, respectively (given in standard tables [7]), F_r and F_a – bearing radial and axial load (radial and axial components of actual bearing load), respectively.

In the case of deep groove ball bearing loaded with pure radial external load F_r, the equivalent load is

$$P_r = F_r. \quad (4)$$

2.2. Adjusted rating life

The adjusted bearing life is actually the basic rating life, given by Eq.(1), adjusted for the reliability of (100 - n)%, for special bearing properties and for specific operating conditions:

$$L_{na} = a_1 a_2 a_3 L_{10}, \quad (5)$$

where a_1 is life adjustment factor for reliability, a_2 - life adjustment factor for special bearing properties, a_3 - life adjustment factor for operating conditions.

Values of a_1 factor are given in standard tables [7], depending on required reliability (90…95)%, since values of a_2 and a_3 factors are discussed only. In accordance with contemporary bearing technology, rolling bearings could be made by the use of a special type and quality of material and/or special manufacturing process and/or special design. These special properties are taken into account by the adjustment factor a_2. The values of this factor are mostly based on experience and could be obtained from the bearing manufacturers [7].

The life adjustment factor a_3 takes into account the influence of adequacy of the lubricant and lubrication system, contamination, and conditions causing changes in material properties. The standard recommends that bearing manufacturers provide appropriate values of a_3 in accordance with the specific application and used bearing type.

3. ISO 281:2007

3.1. Modified rating life

The modified rating life equation for the rolling bearing is

$$L_{nm} = a_1 a_{ISO} L_{10}, \quad (6)$$

where L_{10} is basic rating life, given by Eq.1, a_1 - modification factor for reliability, a_{ISO} – modification factor for system approach.

It is important to know that the a_1 values for the reliabilities 95% to 99% have been modified compared with the corresponding values in the ISO 281:1990. Furthermore, the table with a_1 values is extended to 99,95%. In the period between the last two editions of standard ISO 281, a practical method was developed for performing modified life systems approach calculations by introduction a_{ISO} factor. This factor considers the fatigue stress limit of the bearing steel and also the influence of lubrication and contamination on bearing service life.

3.2. Life modification factor a_{ISO}

The life modification factor for a system approach is determined by analytical investigations, empirical laboratory tests and practical experience. Besides bearing type, fatigue load and bearing operational load, the factor a_{ISO} considers the influence of [3]: lubricant (the type of bearing size and speed, lubricant, viscosity, additives); environment (seals, contamination level); contaminant particles (hardness and particle size in relation to bearing size, lubrication method, filtration), and cleanliness during mounting.

The life modification factor a_{ISO} for radial ball bearings can be calculated with equation [3]

$$a_{ISO} = 0.1 \left(1 - \left(2.5671 - \frac{A}{\kappa^B} \right)^{0.83} \left(\frac{e_C C_u}{P} \right)^{\frac{1}{3}} \right)^{-9.3}, \quad (7)$$

where κ is viscosity ratio, e_C - contamination factor, C_u – fatigue load limit, P – dynamic equivalent load, A and B – constants depending on viscosity ratio values (Table 1).

Table 1: *Constants A and B in Eq.7 depending on viscosity ratio κ*

	A	*B*
$0.1 \le \kappa < 0.4$	2.2649	0.054381
$0.4 \le \kappa < 1$	1.9987	0.19087
$1 \le \kappa \le 4$	1.9987	0.071739

Viscosity ratio is given by

$$\kappa = \frac{\nu}{\nu_1}, \quad (8)$$

where ν is the actual kinematic viscosity of the lubricant at operating temperature, ν_1 – reference kinematic viscosity at operating temperature. In the case of greases, these are operating viscosities of the base oil.

The actual kinematic viscosity of the lubricant at operating temperature is estimated based on the operating temperature and the viscosity of applied lubricant at temperature of 40 °C, using diagrams from catalogues of bearing manufacturers [13,14] or oil and grease manufacturers.

The reference kinematic viscosity can be calculated with following equations [3]

$$\begin{aligned} \nu_1 &= 45000 n^{-0.83} D_{pw}^{-0.5} \quad \text{for } n < 1000 \text{ r/min} \\ \nu_1 &= 4500 n^{-0.5} D_{pw}^{-0.5} \quad \text{for } n \ge 1000 \text{ r/min} \end{aligned}, \quad (9)$$

where n is bearing speed, D_{pw} - pitch diameter of ball set (or mean bearing diameter).

The contamination factor e_C takes into account bearing life reduction caused by solid particles in the lubricant film. It is dependent on type, size, hardness and quantity of the particles, on lubricant film thickness (viscosity ratio κ), as well as on bearing size. Its value varies from 0 (very severe contamination) to 1 (extreme cleanliness). In the transition between normal cleanliness

(oil filtered through fine filter; conditions typical of greased and shielded bearing) and slight contamination in the lubricant, contamination factor is about 0.5 [3]. A simplified method to estimate e_C is given in standard using the appropriate qualitative table, but also there is an annex in the standard which provides a more advanced and detailed method to calculate the e_C factor. In accordance with this annex, the contamination factors can be determined for following lubricant methods: circulating online filtered oil, oil bath or offline filtered circulating oil, and grease lubrication. The general formula for the contamination factor is

$$e_C = a\left(1-\frac{E}{D_{pw}^{1/3}}\right); \qquad a = F\kappa^{0.68}D_{pw}^{0.55} \quad \text{with restriction } a \le 1, \tag{10}$$

where E and F are constants depending on lubrication method (Table 2).

Table 2: *Constants C and E in Eq.10 depending on the lubricant method*

	E	*F*
Circulating oil lubrication with online filters		
$\beta_{6(c)}$=200; ISO 4406 code –/13/10	0.5663	0.0864
$\beta_{6(c)}$=200; ISO 4406 code –/15/12	0.9987	0.0432
$\beta_{25(c)}\geq$75; ISO 4406 code –/17/14	1.6329	0.0288
$\beta_{25(c)}\geq$75; ISO 4406 code –/19/16	2.3362	0.0216
Oil lubrication without filtration or with offline filters		
ISO 4406 code –/13/10	0.6796	0.0864
ISO 4406 code –/15/12	1.141	0.0288
ISO 4406 code –/17/14	1.67	0.0133
ISO 4406 code –/19/16	2.5164	0.00864
ISO 4406 code –/21/18	3.8974	0.00411
Grease lubrication		
High cleanliness	0.6796	0.0864
Normal cleanliness	1.141	0.0432
Slight to typical contamination D_{pw} < 500mm	1.887	0.0177
Slight to typical contamination $D_{pw} \geq$ 500mm	1.677	0.0177
Severe contamination	2.662	0.0115
Very severe contamination	4.06	0.00617

The quantity $\beta_{x(c)}$ in Table 2 is the filtration ratio at contamination particle size x in μm according to ISO 16889 ("Hydraulic fluid power filters – Multi-pass method for evaluating filtration performance of a filter element"). The contamination levels for a range of cleanliness codes are defined in ISO 4406 ("Hydraulic fluid power – Fluids – Methods for coding the level of contamination by solid particles").

The fatigue load limit C_u is defined as the load at which the fatigue stress limit σ_u is reached in the contact between the raceway and most heavily loaded ball in bearing. For rolling bearings of commonly used high quality material and good manufacturing quality, the fatigue stress limit is reached at contact stress of approximately 1500 MPa [3]. This stress value takes into account additional stresses caused by manufacturing tolerances and operational conditions, but in many applications actual contact stresses are larger than fatigue stress limit reducing bearing life.

The fatigue load limit C_u for ball bearing is given by

$$C_u = 0.2288ZQ_u \quad \text{for } D_{pw} \le 100 \text{ mm}; \qquad C_u = 0.2288ZQ_u\left(\frac{100}{D_{pw}}\right)^{0.5} \quad \text{for } D_{pw} > 100 \text{ mm}, \tag{11}$$

where Q_u is the fatigue load limit of a single contact.

The fatigue load limit Q_u is the minimum fatigue load limit of the highest loaded contact (contact between the mostly loaded ball and one of the raceways):

$$Q_u = \min\left(Q_{ui}, Q_{ue}\right), \tag{12}$$

where $Q_{ui,\ e}$ are fatigue load limit at a single inner ring raceway contact and a single outer ring raceway contact.

An advanced method for calculating the fatigue load limit C_u is described in [3]. The simplified equations to estimate this quantity are given as well:

$$C_u = \frac{C_0}{22} \quad \text{for } D_{pw} \le 100 \text{ mm}; \qquad C_u = \frac{C_0}{22}\left(\frac{100}{D_{pw}}\right)^{0.5} \quad \text{for } D_{pw} > 100 \text{ mm}, \tag{13}$$

where C_0 is basic static load rating.

The static load rating for ball bearing can be calculated in accordance with [12]

$$C_0 = f_0 Z D_w^2, \tag{14}$$

where f_0 is the factor which depends on the geometry of the bearing components, given in standard tables.

The results of the simplified estimation of fatigue load limit can differ from the results of advanced method which is preferred [3].

4. Numerical example

A numerical example was made in order to apply a standard method for calculating life modification factor for system approach. The factor a_{ISO} was estimated for four bearings of the same bore diameter (30 mm) and of different series (60, 62, 63 and 64).

Table 3: *Estimation of the life modification factor for the system approach*

	Estim.	**6006**	**6206**	**6306**	**6406**
d, mm	-	30	30	30	30
D, mm	-	55	62	72	90
Z	-	11	9	8	7
D_w	-	7.144	9.525	12.303	16.669
D_{pw}	0.5(d + D)	42.5	46	51	60
D_w/ D_{pw}	-	0.17	0.21	0.24	0.28
f_c	[3]	59.8	59.8	59.0	57.1
b_m	[3]	1.3	1.3	1.3	1.3
C_r, kN	Eq.2	13.2	19.4	28.1	43.0
f_0	[12]	14.7	13.7	13.0	12.1
C_0, kN	Eq.14	8.3	11.2	15.7	23.5
C_u, kN	Eq.13	0.377	0.509	0.714	1.068
P_r, kN	0.5C_r	6.6	9.7	14.05	21.5
ν, mm^2/s	[13,14]	16	16	16	16
ν_1, mm^2/s	Eq.9	21.83	20.98	19.93	18.37
κ	Eq.8	0.7	0.8	0.8	0.9
E	Table 2	1.141	1.141	1.141	1.141
F	Table 2	0.0432	0.0432	0.0432	0.0432
a	Eq.10	0.2665	0.3049	0.3227	0.3823
A	Table 1	1.9987	1.9987	1.9987	1.9987
B	Table 1	0.19087	0.19087	0.19087	0.19087
e_C	Eq.10	0.1794	0.2078	0.2234	0.2709
$\boldsymbol{a_{ISO}}$	Eq.7	**0.285**	**0.331**	**0.337**	**0.364**

The external geometry parameters (bore diameter and outside diameter) of these bearings are known from the manufacturer's catalogues [13,14]. The authors of this paper have the appropriate data of internal geometry (number and diameter of balls in considered bearings). Based on these geometric parameters, the standard dynamic and static load ratings were determined (Table 3). All bearings are subjected to the same relative load (half of its own dynamic load capacity). The lubricant is the grease of normal cleanliness. The viscosity of base oil at 40 °C is 80 mm^2/s. It is assumed that the operating temperature is 80 °C and the operating bearing speed is 1000 rpm.

Based on the results shown in Table 3, it can be concluded that under the same operating conditions, the contamination factor e_C and the life modification factor a_{ISO} increase with increasing series of bearings due to the influence of the rolling element size and fatigue load limit. The values of the life modification factor are 0.285…0.364 depending on the bearing series. This means that the reduction of the modified rating life in relation to the basic service

life is approx. (64…72)% even in the case of normal lubricant cleanliness (!). Therefore, the factor a_{ISO} must always be taken into the account in the calculation of the bearing service life.

A comparative overview of the calculation of bearing basic and modified rating life according to ISO and two bearing manufacturers is given i Table 4.

Table 4: *Deep groove ball bearing life comparison*

	Estim.	**6006**	**6206**	**6306**	**6406**
ISO 281:2007					
C_r, kN	Eq.2, T.3	13.2	19.4	28.1	43.0
C_0, kN	Eq.14, T.3	8.3	11.2	15.7	23.5
C_u, kN	Eq.13, T.3	0.377	0.509	0.714	1.068
C_0/C_u	-	22	22	22	22
a_{ISO}	Eq.7, T.3	0.285	0.331	0.337	0.364
P_r, kN	$0.5C_r$ *	6.6	9.7	14.05	21.5
L_{10}, 10^6	Eq.1	8	8	8	8
$L_{m\,10}$, 10^6	Eq.6	**2.28**	**2.65**	**2.70**	**2.91**
Manufacturer A					
C_r, kN	Catalogue	13.8	20.3	29.6	43.6
C_0, kN	Catalogue	8.3	11.2	16	23.6
C_u, kN	Catalogue	0.355	0.475	0.670	1.000
C_0/C_u	-	23.4	23.6	23.9	23.6
a_{ISO}	Eq.7	0.281	0.322	0.328	0.393
P_r, kN	(*)	6.6	9.7	14.05	21.5
L_{10}, 10^6	Eq.1	9.14	9.17	9.35	8.34
$L_{m\,10}$, 10^6	Eq.6	**2.57**	**2.95**	**3.07**	**3.28**
Manufacturer B					
C_r, kN	Catalogue	12.7	19.3	29	42.5
C_0, kN	Catalogue	8.0	11.2	16.3	25
C_u, kN	Catalogue	0.390	0.680	1.020	1.640
C_0/C_u	-	20.5	16.5	16.0	15.2
a_{ISO}	Eq.7	0.291	0.378	0.398	0.514
P_r, kN	(*)	6.6	9.7	14.05	21.5
L_{10}, 10^6	Eq.1	7.12	7.88	8.79	7.72
$L_{m\,10}$, 10^6	Eq.6	**2.07**	**2.98**	**3.50**	**3.97**

There are some differences in load ratings and fatigue load limit, because actual bearing designs, based on the expertise of the manufacturer can deviate from standard reference geometrics, as well as used steel of specific quality. Consequently, there are differences in estimated basic and modified service life. This numerical example showed that there are no large deviations in the calculation procedures proposed by the bearing manufacturers in relation to the standard recommendations. Even more, there is only a slight difference in the results of the bearing life assessment from different manufacturers of the same rank and product quality in the bearing market.

5. ISO/TS 16281:2008

The last version of International Standard on rolling bearings dynamic load ratings and rating life was issued in 2007. In this edition, recommended calculation method for rolling bearing service life takes into account influences of reliability, lubrication, contamination, internal stresses from mounting, hardening, and the fatigue load limit of the material. It is, therefore, possible to determine bearing service life in a more complete way than before. However, the calculation method given in ISO 281:2007 do not consider the objectively present influence of internal clearance and rings tilting or misalignment on bearing service life. For this purpose, the document ISO/Technical Specification 16281, issued in 2008, describes an advanced calculation method, which covers influencing parameters additional to those described in ISO 281: tilting or misalignment, operating clearance of the bearing and internal load distribution on rolling elements. The Technical specification [10] is applied to radial ball bearing, subjected to radial and axial load and roller bearings subjected to pure radial load, both with radial clearance, edge stress and tilt. However, this document does not consider a radial ball bearing with radial clearance subjected to pure radial load, which is a common case in bearing arrangements. The proposed calculation method is not complete and cannot be applied by the user of this Technical Specification. Thereby some quantities in the proposed mathematical model can be solved only by iteration, using computer support. Regardless of this, it is significant information for the user that these influences exist and should not be negligible, as well as it is a theoretical background and basis for further development of calculation procedure considering new influences. Even more, it is stated in the Scope of [10] that it is primarily intended to be used for computer programs and that only together with ISO 281 covers the information needed for life calculations. It is recommended that either this Technical Specification or advanced computer calculations provided by bearing manufacturers, for determining the dynamic equivalent reference load under different loading condition, be used.

6. Conclusion

From 1962 to 2008, a major step was made in bearing service life calculation, by introduction modification factors. The influence of reliability other than 90%, lubrication, contamination and fatigue load limit is very well covered, which is confirmed by significant values of these factors. The influences of load distribution, internal clearance and misalignment on bearing service life has also been identified but has not been quantified through any additional life modification factors. The Technical Committee for rolling bearings is supposed to be very active and surely we could expect in next version of ISO 281 that standard formula for the rating life will be modified by additional factors for the all newly identified impacts.

7. References

1. ISO/TR 8646, Explanatory notes on ISO281/1-1977, (1985)
2. ISO/TR 1281-1, *Rolling bearings – Explanatory notes on ISO 281 – Part 1: Basic dynamic load rating and basic rating life*, (2008)
3. ISO 281, *Rolling bearings – Dynamic load ratings and rating life*, (2007)
4. A. Palmgren, *On the carrying capacity and life of ball bearings*, Ball Bearing Journal, 034, 34-44 (1937)
5. G. Lundberg, A. Palmgren, *Dynamic capacity of rolling bearings*, Acta Polytechnica Mechanical Engineering Series, Royal Swedish Academy of Engineering Sciences, Vol.1, No.3, 7 (1947)
6. G. Lundberg, A. Palmgren, *Dynamic capacity of rolling bearings*, Acta Polytechnica Mechanical Engineering Series, Royal Swedish Academy of Engineering Sciences, Vol.1, No.4 (1952)
7. ISO 281, *Rolling bearings – Dynamic load ratings and rating life*, (1990)
8. ISO/TS 16799, *Rolling bearings – Dynamic load ratings and rating life – Discontinuities in the calculating of basic dynamic load ratings*, (1999)
9. ISO/TR 1281-2, *Rolling bearings – Explanatory notes on ISO 281 – Part 2: Modified rating life calculation, based on a system approach to fatigue stresses*, (2008)
10. ISO/TS 16281, *Rolling bearings – Methods for calculating the modified reference rating life for universally loaded bearings*, (2008)
11. T. Lazović, R. Mitrović, M. Ristivojević, *Influence of internal radial clearance on the ball bearing service life*, J Balk Tribol. Assoc, 16 (1), 1-8 (2010)
12. ISO 76, *Rolling bearings – Static load ratings*, (2006)
13. INA/FAG, *Rolling bearings*, HR1, Schaeffler Group, (2008)
14. SKF, *General catalogue*, 6000 EN, (2005)

Acknowledgement

This work was supported by the Ministry of Education, Science and Technological Development of the Republic of Serbia (Contract No. 451-03-68/2020-14/200135).

3-phase motor speed regulator based on microcontroller and intelligent power driver controller

Assos. prof. Dr. Eng. Stefanov G.[1], Assist. prof. Dr. Eng. Cekerovski T.[2], Assist. M.Sc. Citcuseva Dimitrova B.[3], Grad.stud. Stefanova S.[4]

Faculty of Electrical Engineering, University ''Goce Delcev''-Stip, Macedonia[1,2,3]
Faculty of Computer Science and Engineering, University ''Ss Cyril and Methodius''-Skopje, Macedonia[4]
goce.stefanov@ugd.edu.mk, todor.cekerovski@ugd.edu.mk, biljana.citkuseva@ugd.edu.mk, sara_stefanova@hotmail.com

Abstract: *This paper describes the design and practical implementation of speed controller for 3-phase induction motor based on ATmega 2560 microcontroller. Based on the theoretical analysis of the induction motor, are defined the requirements that the controller should satisfy them. Then, based on the specificity of the selected controller, the operating mode of the ATmega 2560 controller is designed. The specificity of this solution is that the driver circuit, which is connected between the controller and the motor, is realized with an intelligent power controller. Finally, the results of the practical work of this motor controller are given.*

***KEYWORDS**: 3-PHASE MOTOR REGULATOR, ATMEGA 2560, INTELLIGENT POWER CONTROLLER*

1. Introduction

In modern industrial power plants the tendency is to use induction motors controlled by V/F converters. The main reason for this in terms of the motor is the advantage which offered by induction motors, primarily in terms of DC motors, and in terms of the converter is the need to regulate the speed of the motor and thus its power. This ensures that the motor runs at the speed and power required by the operating process [1], [2], [3], [4].

There are a number of methods of speed control of an induction such as pole changing, frequency variation, variable rotor resistance, variable stator voltage, constant V/f control, slip recovery method etc. The constant V/f speed control method is the majority generally used. In this method, the V/f ratio is kept constant which in turn maintains the magnetizing flux constant so that the maximum torque remains unchanged. Thus, the motor is totally utilized in this method [5], [6].

In this paper, the main emphasis is on the work of the microcontroller and the driver's circuit, ie. power converter. The microcontroller generates a 3-phase SPWM signal that provides V/F operation of the motor [7]. In the paper, the power converter is realized in an integrated technique, so-called intelligent power module (IPM).

2. SPWM Microcontroller and Intelligent Power Module

Guided by the main goal of the paper, implementation of the microcontroller in generating SPWM signals and realization of the converter with intelligent power module (IPM), here will be explained the functioning of these three interconnected parts, ie. SPWM, microcontroller and IPM.

In the Fig. 1 is shown a block diagram on 3-phase motor which is controlled by microcontroller.

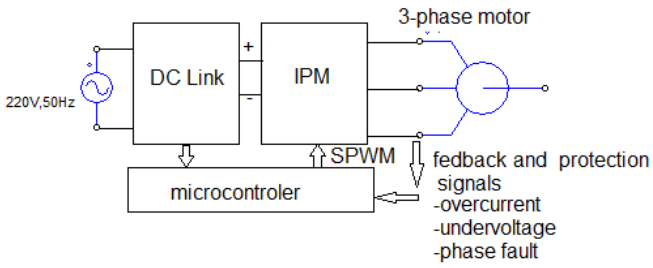


***Fig. 1** Block diagram on 3-phase motor controlled by microcontroller.*

2.1 SPWM signal

Here we take a look over the concepts of SPWM signal which is a width modulated signal but with certain values on such a way that we could create a sine shape wave at the output. This with used on MOSFET or IGBT transistors could result in a sine wave inverter.

It is generally known that PWM signal is pulse width modulation. That means we modulate the width of a square signal and by that we could control power. But, this width in case of normal PWM is always the same. In case of SPWM or sinusoidal pulse width modulation, the width of the signal is increasing and decreasing and my that simulating the curve of the sine wave. With small width pulse, the output will increase a little bit and that represents the zone after the 0 cross of the sine wave. Then with bigger widths, the output is getting bigger and bigger and then it starts to get lower, just as a sine wave. Using two transistors switching, can could get both the positive and negative sides of the sine wave, Fig. 2.

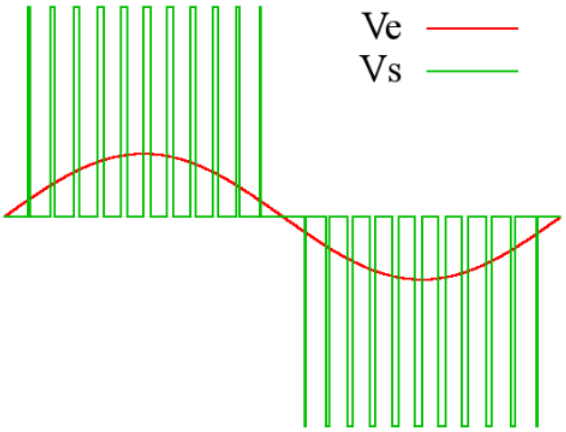


***Fig. 2** Construction of SPWM signal.*

In the Fig. 3 below can see a bit better how the width of the SPWM can create a good sinusoidal shape at the output. Will use the microcontroller to generate this SPWM signal. We apply this signal to the intelligent power module driver. These will be connected to the motor. In the Fig. 3 is shown SPWM signal and the current and voltage waveforms of the motor.

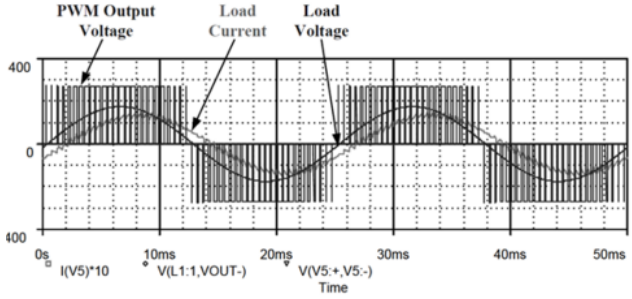


***Fig. 3** SPWM signal and the current and voltage waveforms of the motor.*

2.2 Microcontroller

The main task of the microcontroller is to generate SPWM signals [8]. Because the motor is three-phase, the controller needs to generate two asymmetric outputs for each phase. So microcontroller needs generate three phase SPWM signals. These signals will be connected to the inputs of the intelligent power converter.

Because Atmega 328P microcontroller on arduino uno board has three timers and one of them is used for interrupt it can not be used. Therefore here is used an Atmega 2560 microcontroller embedded on arduino mega board. Arduino mega 2560 board have five timers and 15 PWM capable pins [9]. The basic features of this controller are:

Micro-controller	ATmega2560	
	Operating Voltage	5V
	Input Voltage (recommended)	7-12V
	Input Voltage (limits)	6-20V
	Digital I/O Pins	54 (of which 14 provide PWM output)
	Analog Input Pins	16
	DC Current per I/O Pin	40 mA
	DC Current for 3.3V Pin	50 mA
	Flash Memory	256 KB of which 4 KB used by bootloader
	SRAM	8 KB
	EEPROM	4

In Fig. 4 is shown microcontroller Atmega2560, used in arduino mega board.

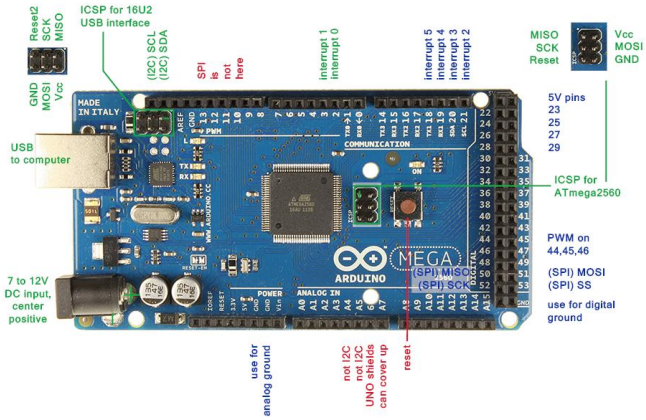


Fig.4 *Microcontroller Atmega 2560 used in arduino mega board.*

To solve our task, generating three SPWM signals requires knowledge of the microcontroller timers. So we'll see the corresponding between timers and pins:

-Timer 0-pin 4 (OC0B) and pin 13(OC0A)
-Timer 1-pin 11(OC1A) and pin 12(OC1B)
-Timer 2-pin 9(OC2B) and pin 10(OC2A)
-Timer 3-pin 2(OC3B), pin 3(OC3C) and pin 5(OC3A)
-Timer 4-pin 6(OC4A), pin 7(OC4B) and pin 8(OC4C)
-Timer 5-pin 44(OC5C), pin 45(OC5B) and pin 46(OC5A)

Timer 1 is used for , Timer 0 for first phase, Timer 2 for the second phase and Timer 3 for the third phase with OCxA for positive half duty cycle and OCxB for the negative half duty cycle like in the Fig. 5 [10].

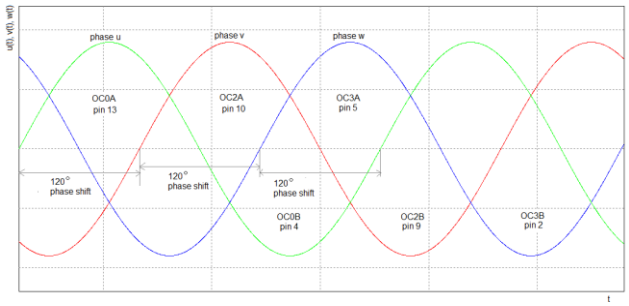


Fig. 5 *Condition of the registers OCxA and OCxB (x = 0, 2, 3) on pins 13, 10, 5 and 4, 9, 2.*

If for 180 degrees we have 314 elements, for 120 degrees we have 209 elements so the second signal must start when the first is at 209 pulse and the third must start when the second is at 209 pulse.

So, when the program starts, the interrupt is enabled and first is executed the first signal part (with element i). When i take the 209 value the second signal is enabled (with element j). When j takes the 209 value the third signal is enabled. In this way these three signals are at 120 degrees phase shift.

To ensure the phase shift we use an "if" function and for the second wave is like below:

"if ((i==209) || OK1==1){ OK1=1;"

When "i" has 209th value the "if" function is enabled and everything in it is executed. To mantain the execution of that part for the second signal after the value of i(209) is changed we use a variable which enables the "if" function continuously.

For the third signal the if function is like below:

"if ((j==209) || OK3==1){ OK3=1;"

In this case, the third signal is enabled when "j" (the element for the second signal) has the 209th value. After that, the "if" function is executed like for the second signal.

The waveforms that illustrate the last explanation will be given below in the text.

2.2 Intelligent Power Module Driver

In power electronics, in recent decades, usually in controlling of the motor (not only induction but also DC motors), the connection between the controlling part (in the case is microcontroller) and the motor has been realized with a discreet driver circuit and power bridge converter realized with MOSFET or IGBT transistors [11]. One such solution is shown in the Fig. 6.

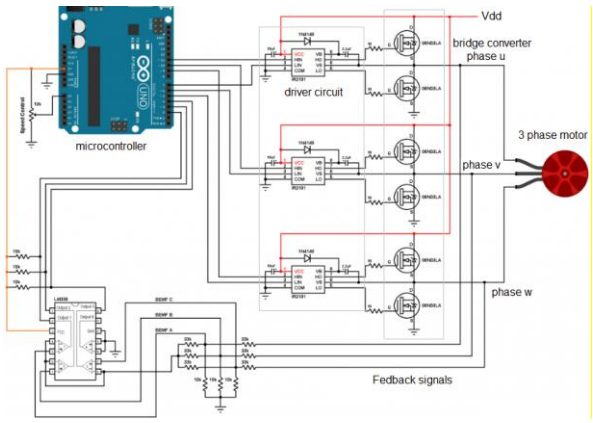


Fig.6 *Controller with discreet driver circuit and bridge converter.*

In recent years, the direction of development and application of intelligent controllers has been practiced not only for control electronics but also for the driver circuit [12]. These intelligent power controllers consist of a driver circuit and a bridge converter. In this

way the hardware construction of the device is facilitated and the protection functions are improved.

In the Fig. 7 is shown motor speed controller controlled with microcontroller and intelligent power module.

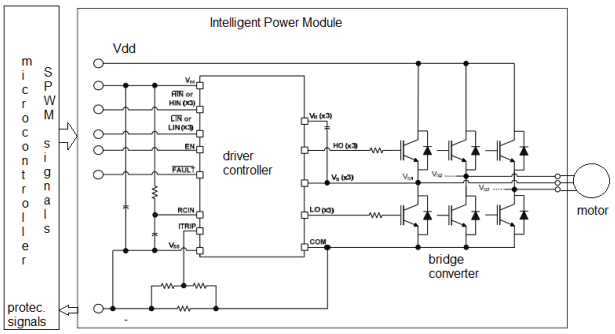


Fig. 7 *Motor controller controlled with microcontroller and intelligent power module.*

3. Design of Speed Regulator

To design the task in the paper we use microcontroller Atmega 2560 in arduino mega board and monolithic intelligent motor controller MC3PHAC (product of Motorola) embedded in intelligent power module TM35 [12].

MC3PHAC is designed specifically to meet the requirements for low-cost, variable-speed, 3-phase ac motor control systems. The device is adaptable and configurable, based on its environment. It contains all of the active functions required to implement the control portion of an open loop, 3-phase ac motor drive. One of the unique aspects of this device is that although it is adaptable and configurable based on its environment, it does not require any software development. This makes the MC3PHAC a perfect fit for customer applications requiring ac motor control but with limited or no software resources available. The device features are:

- Volts-per-Hertz speed control
- Digital signal processing (DSP) filtering to enhance speed stability
- 32-bit calculations for high-precision operation
- Internet enabled
- No user software development required for operation
- 6-output pulse-width modulator (PWM)
- 3-phase waveform generation
- 4-channel analog-to-digital converter (ADC)
- User configurable for standalone or hosted operation
- Dynamic bus ripple cancellation
- Selectable PWM polarity and frequency
- Selectable 50/60 Hz base frequency
- Phase-lock loop (PLL) based system oscillator
- Serial communications interface (SCI)
- Low-power supply voltage detection circuit.

Included in the MC3PHAC are protective features consisting of dc bus voltage monitoring and a system fault input that will immediately disable the PWM module upon detection of a system fault.

Some target applications for the MC3PHAC include:

- Low horsepower HVAC motors
- Home appliances
- Commercial laundry and dishwashers
- Process control
- Pumps and fans.

In the Fig. 8 is shown the block diagram of IPM TM35 with built motor controller MC3PHAC, and on the Fig. 9 is shown the appearance of real IPM TM35.

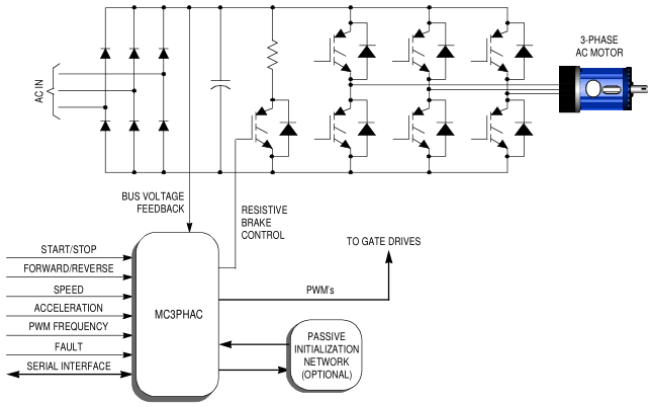


Fig. 8 *Block diagram of IPM TM35 with built motor controller MC3PHAC.*



Fig. 9 *Appearance of real IPM TM35.*

In the Fig. 10 is shown block diagram on speed motor regulator based of microcontroller Atmega 2560 and intelligent power module TM 35.

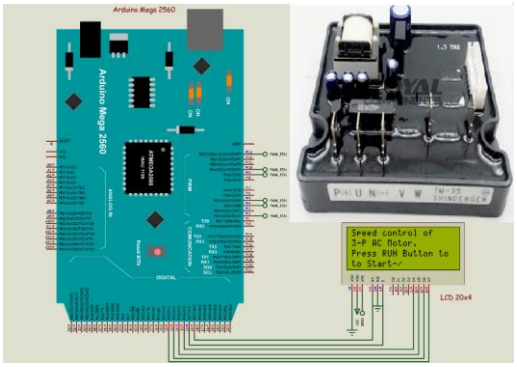


Fig. 10 *Block diagram on speed motor regulator based of microcontroller Atmega 2560 and intelligent power module TM 35.*

From the Fig. 10 can be see that is used LCD display 2004 on which the modes of operation of the regulator are visualized.

4. Experimental results

In the Fig. 11 is shown experimentally test the circuit of motor speed regulator.

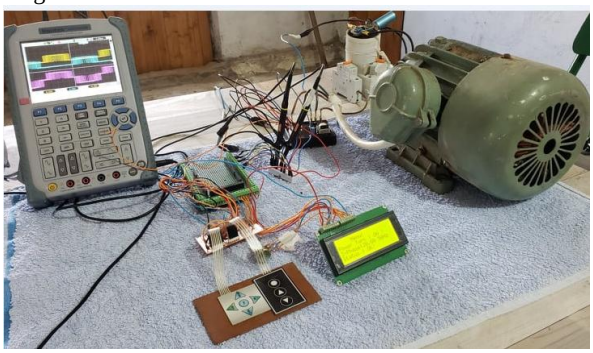


Fig. 11 *Experimentally test the circuit of motor speed regulator.*

In the Fig. 12 are shown waveforms on the PWM signals from the microcontroller for SPWM frequency (switching frequency) 4 kHz and motor frequency 19 Hz.

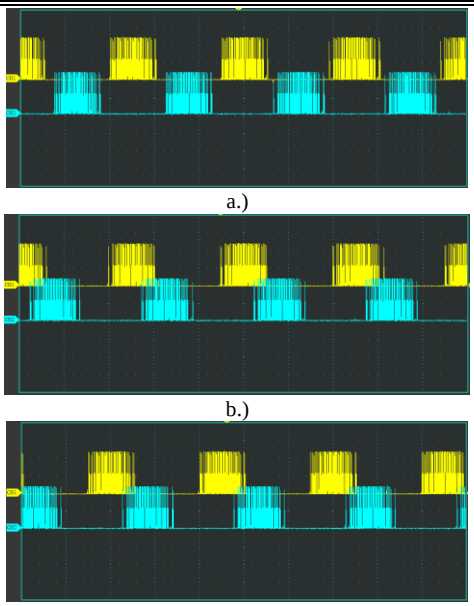


Fig. 12 *Waveforms on theS PWM signals from the microcontroller: a.) PWM signals on phase u pin 4 (channel 1) and pin 13 (channel 2), b.) SPWM signals on phase u pin 4 (channel 1) and phase v pin 9 (channel 2), c.) SPWM signals on phase v pin 9 (channel 1) and phase w pin 2 (channel 2), Ch1 = 2 V/div, Ch2 = 2 V/div, time = 2 mS/div.*

From the Fig. 12 a.) can be seen that the PWM signals on one phase (in case phase u) are shifted by 180° and that there is a dead between the failling and the rising edge of the signals. From Fig. 12 b.) and Fig. 12 c.) can be seen that SPWM signals on phase u pin 4 (channel 1) and phase v pin 9 (channel 2) are shifted by 120°, and SPWM signals on phase v pin 9 (channel 1) and phase w pin 2 (channel 2) are also shifted by 120°.

In the Fig. 13 is shown waveforms on SPWM signals on phase u pin 4 (channel 1) and phase v pin 9 (channel 2) for illustration on the SPWM switching (f_s = 4 kHz) and motor frequency (f = 50 Hz).

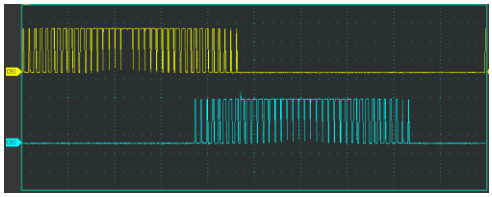


Fig. 13 *Waveforms on SPWM signals on phase u pin 4 (channel 1) and phase v pin 9 (channel 2) for illustration on the SPWM switching (f_s = 4 kHz) and motor frequency (f = 50 Hz).*

From the Fig. 13 can be seen that SPWM switching frequency is f_s = 4 kHz (T_s = 250 µS), and motor frequency in case is maximal f = 50 Hz (T = 20 mS). The number of SPWM pulses per half-period is 40. SPWM signals with such waveforms will provide phase voltages to the motor displaced by 120°.

On the channel 1 in the Fig. 14 is shown waveform of the phase voltage u, and of the channel 2 is shown waveform of the phase voltage v for motor frequency 50 Hz.

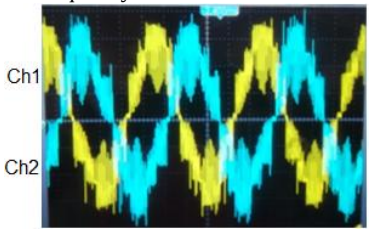


Fig. 14 *Waveform of line voltage: on the channel 1 is the phase voltage u, and on the channel 2 is the phase voltage v for motor frequency 50 Hz, Ch1 = 100 V/div, Ch2 = 100V/div, time = 4 mS/div.*

In Table I are given dates for effective values of the phase voltage of the motor U_{eff} for different motor frequency f.

Table I: *Effective values of phase motor voltage U_{eff} for different motor f frequency.*

U_{eff}(V)	10.8	39.3	65.55	91	110.05	133.20	152.04	179
f(Hz)	3	11	19	26	31	37	42	50
U_{eff}/f	3.60	3.57	3.45	3.50	3.55	3.60	3.62	3.58

In the Fig. 15 is shown the ratio of the effective value of the phase voltage of the motor and the motor frequency (U_{eff}/f) obtained by measuring on the developed prototype of the speed motor regulator.

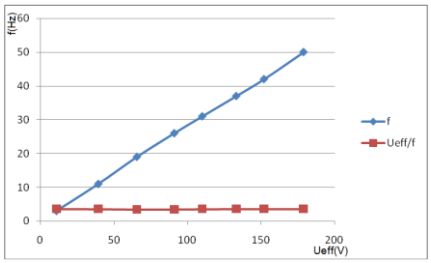


Fig. 15 *Ratio of the effective value of the phase voltage of the motor and the motor frequency (U_{eff}/f) obtained by measuring on the developed prototype of the speed motor regulator.*

From the dates in Table I and the Fig. 15 can be seen that the ratio of the effective value of the phase voltage to the motor and the frequency (U_{eff}/f) is maintained constant by applying the solution in the paper. Maintaining a constant ratio U_{eff}/f means that the flux i.e. the moment of the motor is constant.

5. Conclusion

In this paper is design and practically realized V/F speed regulator for 3-phase induction motor based on microcontroller. The specificity of the solution in the paper is the use of an intelligent power module for the power converter. Experimental results from the operation of the designed motor speed regulator show that it provides operation of the motor with a constant V/F ratio. This maintains the constant flux i.e. the moment of the motor.

References

[1] W. B. Williams, Principles and Elements of Power Electronics, University of Strathclyde, Glasgow, 2006.

[2] Taufik, and Dolan, Advanced Power Electronics, 5th Revision. Cal Poly State University, San Luis Obispo, 2011.

[3] N. Mohan, T. M. Undeland & W. P. Robbins, Power Electron ics: Converters, Applications, and Design. John Wiley & Sons, 2003.

[4] W. Shepherd & Li Zhang, Power Converter Circuits. Marcel Dekker, 2004.

[5] O. D. Muñoz, Design Strategy for a 3-Phase Variable Frequecy Drive (VFD), California Polytechnic State University, San Luis Obispo, 2011.

[6] https://www.electricaleasy.com/2014/02/speed-control-methods-of-induction-motor.html

[7] D. Maksimovic, R. Zane, R. Erickson, "Impact of digital control in power electronics", *In Proceedings of the IEEE 16th International Symposium on Power Semiconductor Devices and ICs.* May: 13–22. 2004.

[8] https://github.com/carneeki/OpenVFD, Variable Frequency Drive for ATmega328 based Arduino.

[9] Atmel-2549Q-AVR-ATmega640/V-1280/V-1281/V-2560/V-2561/V-Datasheet_ Atmel Corporation 1600 Technology Drive, San Jose, CA 95110 USA 02/2014.

[10] PSpice 9.1, simulation program, http://pspice.softonic.com.br

[11] www.irf.com.International Rectifier, datasheet IR2101(-1 2)(S)PbF/IR2113(-1-2)(S)PbF.

[12] Motorola, 3-Phase AC Motor Controller MC3PHAC/D Rev. 1, 4/2002.

Evolution of creative thought with elements of artificial intelligence on example of synthesis of clamping mechanisms

Kuznetsov Yuri
National Technical University of Ukraine "igor Sikorsky Kyiv Politechnic Institute", Kiyv, Ukraine,03056,Pobeda av.37

Abstract. *History of gradual increase of elements of artificial intelligence is resulted in the process of creative thought at creation of on principle new structures and charts of clamping cartridges on the example of cangovykh. Thinking process on on the lasts of peat-time of application of artificial intelligence presented as a binary koda and waves of frequency impulses, reminding cerebration.*
KEY WORDS: *CREATIVE THOUGHT, ARTIFICIAL INTELLIGENCE, COLLETS, EVOLUTION, CLAMPING MECHANISM.*

Problem statement. The main feature of modernity is the challenges induced to humanity by the fourth industrial revolution, Industry 4.0 [8] with a focus on artificial intelligence and the integration of science, education, manufacturing and the social sphere to achieve goals such as: 1-productivity increase; 2-quality improvement; 3-reduction of energy and raw material costs while preserving the environment; 4-reduction and facilitation of manual labour; 5-facilitation and reduction of routine mental work; 6-expansion of functional and technological capabilities of equipment during modernization. Not everyone clearly understand the challenges of time, holding the progress back. However, devastatingly criticized previously, cybernetics and genetics have paved the way for the new knowledge and its interdisciplinary application in the creation of new techniques and new technologies. New scientific ideas and inventions, as a rule, are in the short term attempted to be implemented into the national economy and social sphere to increase the well-being and quality of life. The solution of this acute problem in the absence of complete information forces to intensify the process of creative thinking through the use of artificial intelligence systems [1,7,12,13,15,18,23]. The process of creative thinking is associated with many obstacles, since the problem of thinking has no unambiguous interpretation and covers a wide range of actions for the left and right hemispheres of the human brain from alternative-logical to intuitive-practical thinking. Regarding clamping mechanisms (CM) with compact collets (CC), creative thinking was aimed at finding technical solutions (fig.1) in the creation of the first single-spindle and multi-spindle auto lathes at the end of the XIX century [20,22,24].

Analysis of latest research and publications. The range of issues related to artificial intelligence is infinitely wide and cannot be covered in one work. Therefore, in this paper, the subject matter is the limited scope of creative activity, being associated with clamping chucks and, in particular, collets, which are widely used in auto lathes for clamping rods, pipes and workpieces [17,20,22,24]. In addition, collets and collet chucks are used not only in various machines and technological equipment, but in everyday life, medicine, etc.

The author's rich experience and interdisciplinary approach together with using the evolution theory [2,5,21], advances in genetics [6], cybernetics [3,4], creatology [14] and creativity methodology [1], where, along with associative and algorithmic methods, system-morphological approach [1,9,25] occupies a large part of the search for solutions, allowed getting closer to the real understanding of the brain and the action of its right hemisphere in a short term, starting from ideas that, at first glance, seem bizarre. are in the short term attempted to be implemented into the national economy and social sphere to increase the well-being and quality of life. The solution of this acute problem in the absence of complete information forces to intensify the process of creative thinking through the use of artificial intelligence systems [1,7,12,13,15,18,23]. The process of creative thinking is associated with many obstacles, since the problem of thinking has no unambiguous interpretation and covers a wide range of actions for the left and right hemispheres of the human brain from alternative-logical to intuitive-practical thinking. Regarding clamping mechanisms (CM) with compact collets (CC), creative thinking was aimed at finding technical solutions (fig.1) in the creation of the first single-spindle and multi-spindle auto lathes at the end of the XIX century [20,22,24].

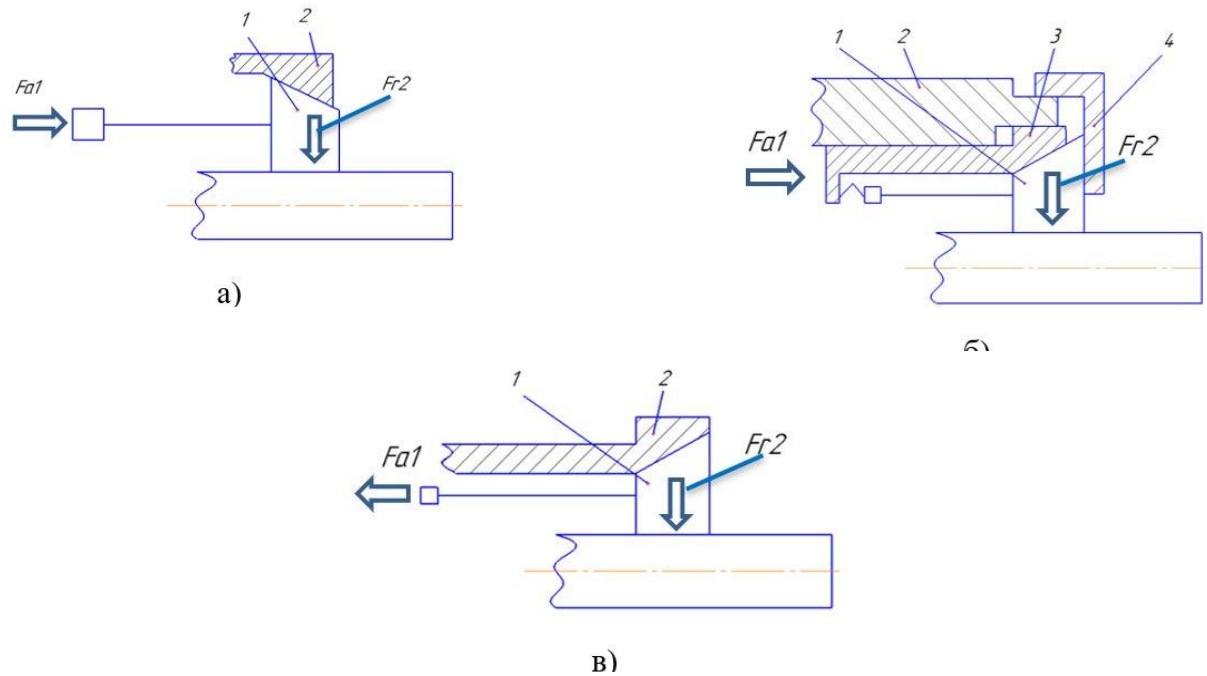


Fig. 1. *Three types of collet chucks of a single clip in auto lathes of the first generation with pressing action (a), with a fixed collet (b), with tightening action (c): 1 - clamp collet; 2 - spindle; 3 - pressure sleeve; 4 - stop nuts*

Task description. The purpose of this work is to trace the stages of evolutionary development and substantiate the principles of creative thinking on the example of the search for clamping chunks (ClC), as a process of creative analysis and synthesis followed by the search for new technical solutions in artificial intelligence systems.

Basic data statement. Starting from the seventh decade of the XX century (fig.2), when a specialized method of finding new technical solutions, called the differential-morphological method of synthesis, was proposed, we are going to trace the stages of creative thinking evolution with increasing elements of artificial intelligence

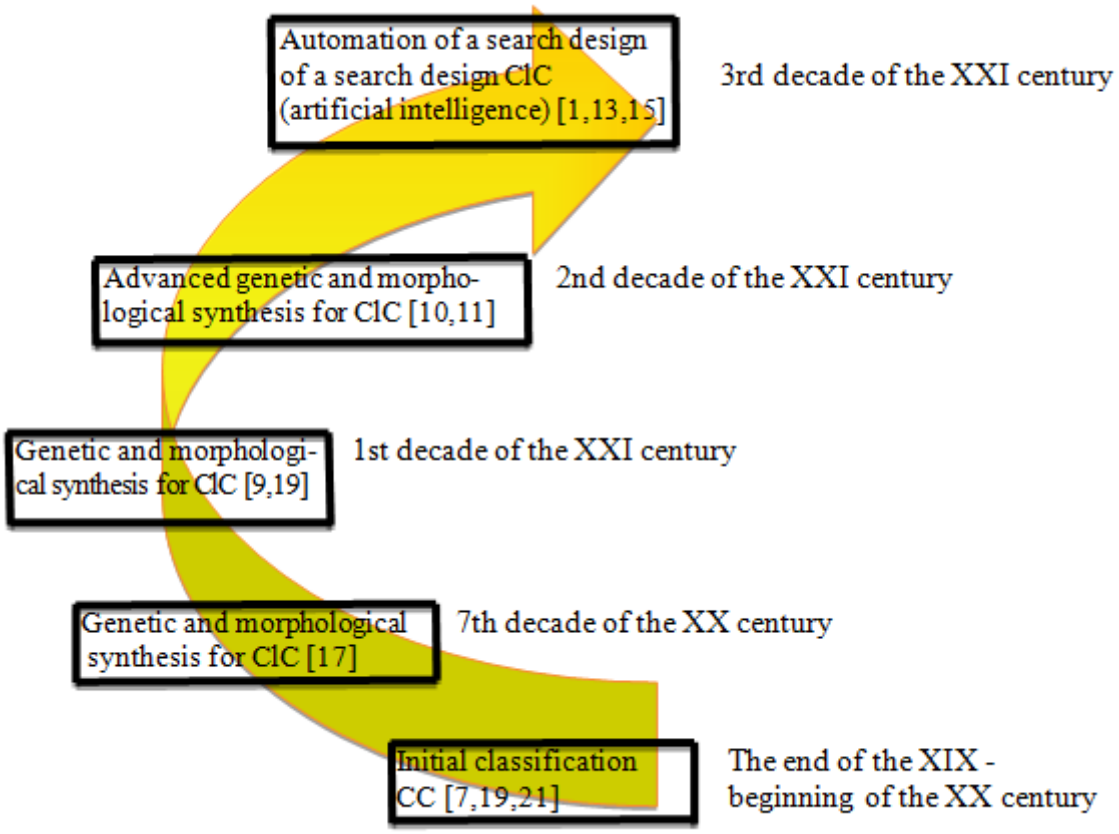


Fig.2. *Evolution of creative thinking in synthesis and genetic prediction of collets and other clamping chucks*

The essence of the differential-morphological method [17] is that to resolve contradictions at the stage of searching for structures (morphology) of the CM and, in particular, ClC, use heuristic techniques of complete, incomplete and combined dismemberment of the clamping element (CE) (fig.3), which gives various main and additional effects, and at unidirectional dismemberment the synthesized structures correspond to new principles of clumping or provide new qualities.

a)

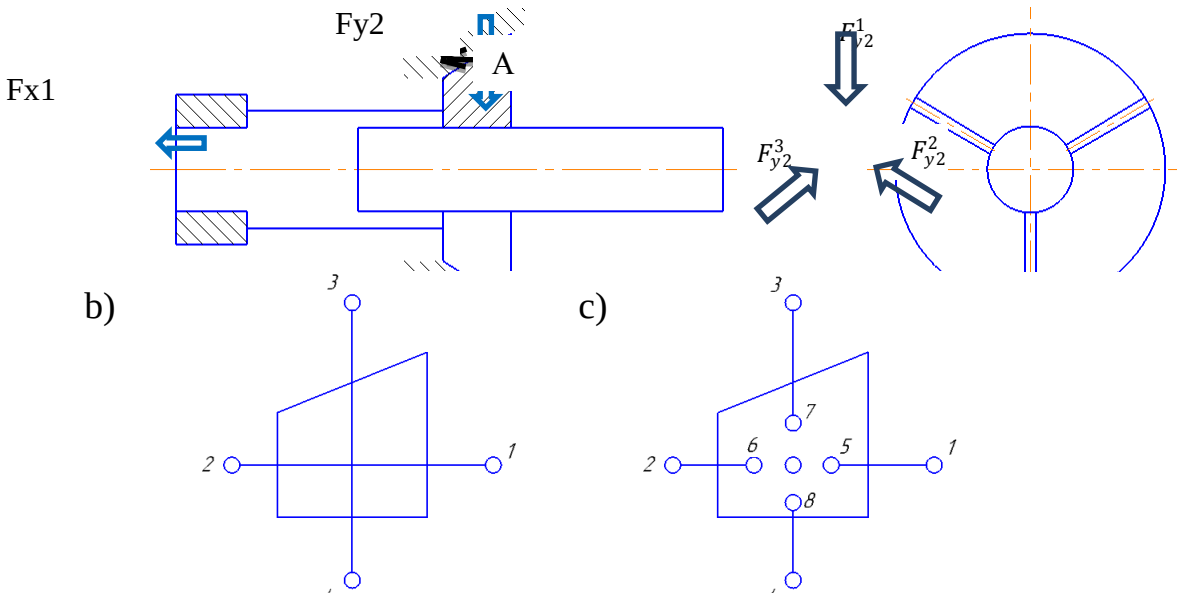


Fig. 3. *Single clamp collet chuck diagram with tightening action (a) and its wedge CE with options for complete (b) and incomplete (c) dismemberment in X, Y planes*

To identify different structures alphanumeric codes of dissections were used, illustrated by the example of complete (fig.4), which gives different effects.

No.	Geometric symbol	Code	
		Alphabetic	Numeric
1	0	X0Y0	0
2		X0X	102
3		Y0Y	304
4		X0Y	203
5		X0Y	204
6		Y0X	301
7		Y0X	401
8		X0Y0Y	20304
9		X0Y0Y	10304
10		X0X0Y	10203
11		X0X0Y	10203.
12		X0X0Y0Y	1020304

Fig. 4. *Complete dissections codes for a wedge clamping element (CE) in XY plane of force action from the clamp drive*

The application of the genetic-morphological approach [8] was oriented towards the clamping of one axisymmetric rotating object with access to the radial and axial clamping principles, which limited the field of search for new solutions. However, the question of simultaneous multi-place clamping of rotating objects fell out of sight, which is widely used in machine tools for processing non-rotating workpieces. One of the first examples of the tangential clamping principle was the invention of the" Collet Chuck" (patent SU N292734), in which holes were made at the end of the collet lips, the axes of which lie in the planes passing through the collet axis and through the middle of the slots forming the petals.

The solution to the problem of simultaneous multi-place clamping of rotating objects with the application of a tangential force offset from the axis of rotation determined the relevance and purpose of these studies. In the direction of the development of previously performed works [5], it is proposed to add to the well-known genetic classification of a single clamp [6] (axial and radial principles with genetic codes $F_1(F_{a1}, F_{r1}, F_{t1})$ - $F_2(F_{a2}, F_{r2})$; M_1 ($M_{a1,}$ $M_{r1,}$ M_{t1}) – $F_2(F_{a2}, F_{r2})$ the tangential principle of single and multi-place clamping with the application of force at the output of the power flow, offset from the axis of rotation by a radius R . At the same time, it appears in addition to the well-known genetic classification [7, 8], which has 48 power flows, another 24 with genetic codes F_1 (F_{a1}, F_{r1}, F_{t1}) - F_2 (F_{t2}); M_1 ($M_{a1,}$ $M_{r1,}$ M_{t1}) – F_2 (F_{t2}). In these studies, the code Fa1 - Ft2 with a wedge transducer (displacement, force, energy) and orientation on the collet clamp (Fig. 5) was selected.

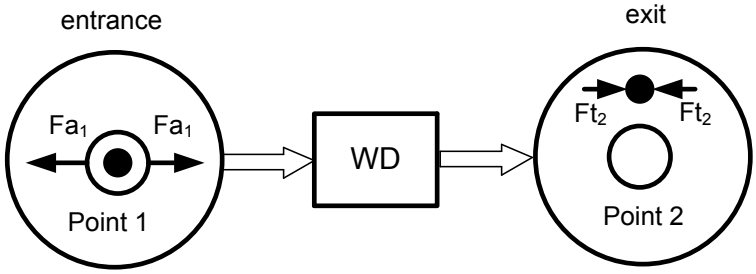


Fig. 5 *Diagram of the transfer of genetic information with a wedge transducer from the input (point 1) to the output (point 2) in a tooling with tangential clamp*

Earlier, based on the analysis of evolutionary development and the long-term use of collet chucks in machine tools in various countries of the world and the process of their mutation [1,4,7,10], the collet chuck with a pulling collet was selected as the most common (Fig. 6, table 1)

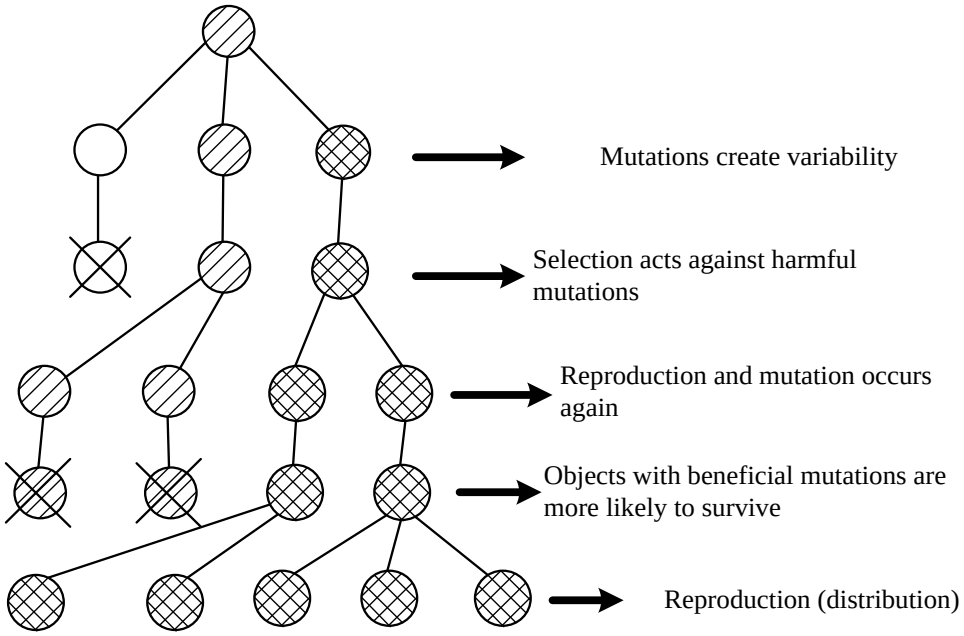
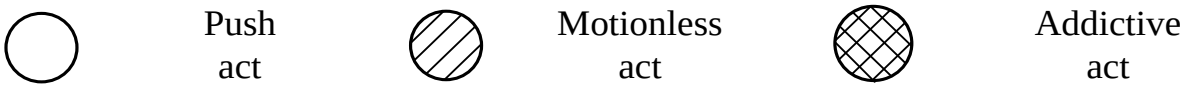
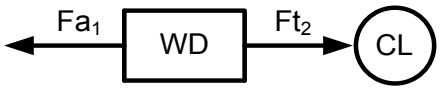
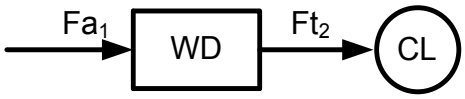
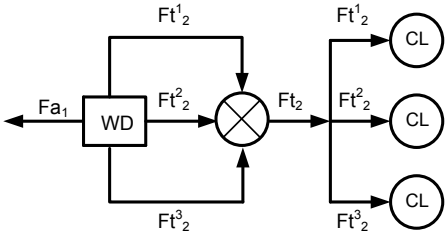
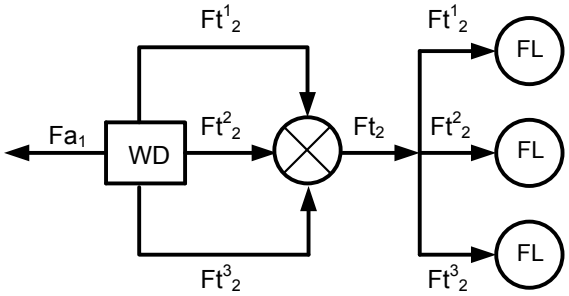


Fig. 6 *Natural selection of single-clamp collet chucks for single-clamping lathes due to mutations with symbols:*



As an example, for the case of the input axial force Fa1 and the output tangential force Ft2, Fig. 5 shows the synthesized instrumental collet mandrel (end mill) with the simultaneous clamping of four cutting inserts. In multilevel genetic modeling and description, the following was taken into account [8, 10]: each level of the structural hierarchy preserves hereditary (genetic) information of a previous level; the structure of an object of an arbitrary level is formed on the basis of structures of previous levels (the higher the level of the hierarchy, the higher the complexity of the object); each object of an arbitrary hierarchy level is represented by a genetic code or structural formula.

Table 1. *Examples of description (modeling) and application of tooling with the tangential principle of a collet clamp*

No. p / p	Structural scheme	Structural genetic formula	Application area
1		F_{a1}–WD–F_{t2}–CL	A clamped cylindrical part or a flying cutter with a long collet is not aligned
2		F_{a1}–WD–F_{t2}–CL	Similar to pos.
3		F_{a1}–WD–$3F_{t2}$–3CL	Simultaneous clamping of three cylindrical parts
4		F_{a1}–WD–$3F_{t2}$–3FL	Simultaneous clamping of three flat tail assembly tool plates (milling cutters, countersinks, reamers)

The description (modeling) with the complexity of the structure and the buildup of genetic information is presented in the form of structural genetic formulas at the following levels:

genetic, $F_{a1;}$ chromosomal, F_{a1} - F_{t2}; object, F_{a1} – $K_{R!}$ F_{t2}; population, F_{a1} – WD - $K_{R!}$ F_{t2}; specific, F_{a1} – WD - $K_{R!}$ F_{t2} -K_{R2} CL (cylindrical shape of the clamping object); F_{a1} – WD - $K_{R!}$ F_{t2} -K_{R2} FL (flat shape of the clamping object)).

The latest model, taking into account the universal genetic replication operator

$K_R = K_{R!} = K_{R2}$ [7,10] is shown in Fig. 7 for various circuits of tooling equipment.

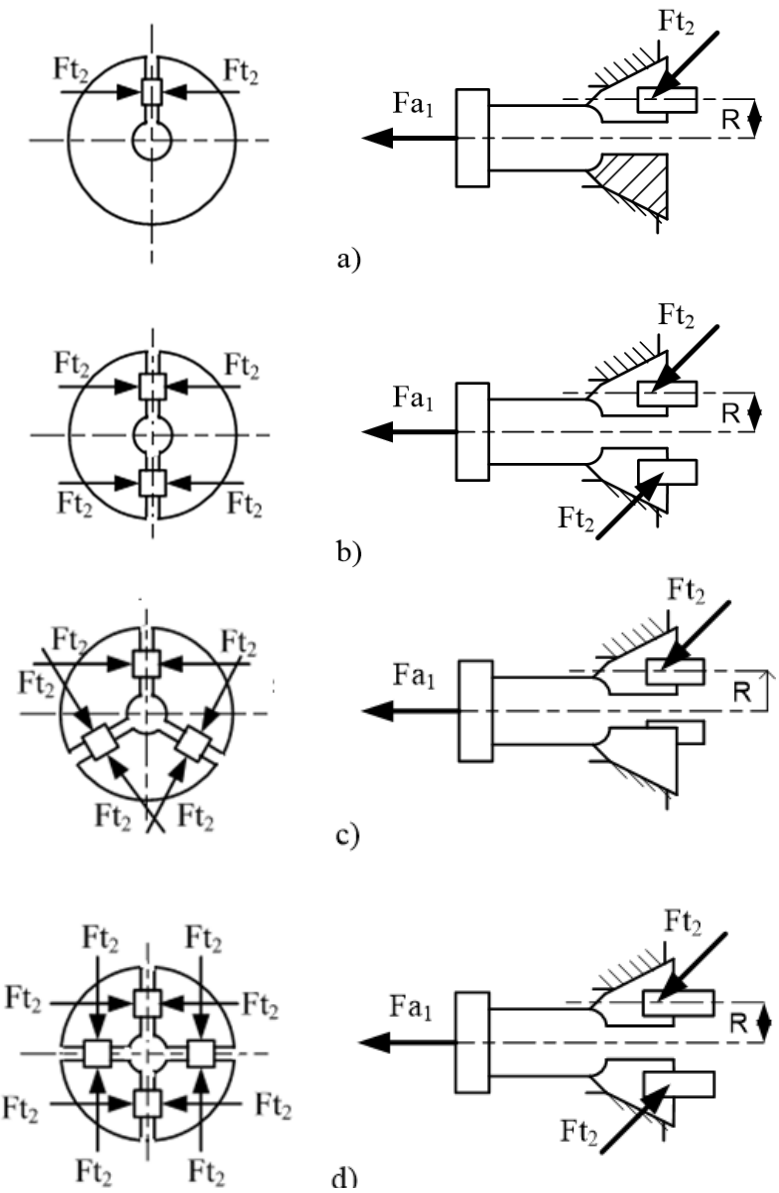


Fig. 7. Schemes of tooling with a collet clamp and genetic formulas at a species level: a) F_{a1} – WD - F_{t2} - FL; b) F_{a1} – WD - 2 F_{t2} -2 FL; c) F_{a1} – WD - 3 F_{t2} -3 FL; d) F_{a1} – WD - 4 F_{t2} -4 FL

One of the ways of creative thinking was an attempt of structural-circuit synthesis and prediction of new CM using a morphological approach and combinatorial algorithms [11], representing combinatorial calculations from a set of special methods and techniques, such as binary presence system or absence of elements in the CM system, being improved or simplified (1 – yes, 0 – no). Starting with the first mechanized axisymmetric CM, which are widely used in lathes, drilling, milling, grinding and multi-purpose machines, there are the following system elements (fig.8): power source (PS), energy converters (EC), clamping drive (CD), clamping chuck (CH), clamping object (CO). The latter can be single, rod, pipe or other workpiece for the manufactured detail, for example, in lathes, or a tool (drill, cutter, grinding wheel, etc.).

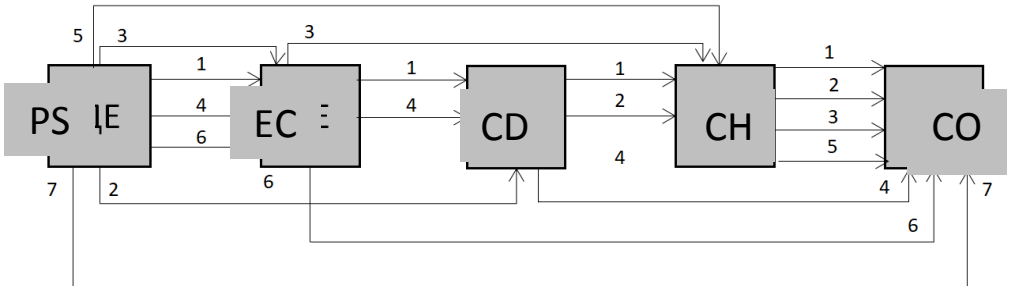


Fig. 8. *Elements of the CM system and connections between them*

In any CM system, there must be an input (power source-weight 1) and an output (clamp object-weight 1). All other elements in the series circuit without taking into account the control system (EC, CD, CH), in fact, according to combinatorics may or may not be present, when it comes to simplifying and reducing the circuit.

According the evolutionary and genetic synthesis theory [2,21] a possibility of 100% prediction and directional synthesis of new CMs using generating systems with a given objective function [19] occurs, which requires complex mathematical transformations with the construction of models for micro- and macroevolutions and writing cumbersome structural genetic formulas [21]. Therefore, the paper proposes a simplified system-morphological approach with the construction of a digital matrix and the gradual removal of system elements in binary coding. Thus, in the evolutionary development of the CM system, only 7 combinations with the following codes can be predicted from the past through the present to the future when searching for all the following variants: CM1-11111, CM2-10111, CM3-11011, CM4-11101, CM5-10011, CM6-11001, CM7-10001. Until now, systems CM1-CM3, and partly CM4 are mainly used in the production. Each code gives a push to search for different options for its implementation.

The expansion and further improvement of the genetic-morphological approach proposed in [9,19] is caused by the requirements of modern tool production and the need to expand the technological capabilities of machine tools based on the modular principle [10]. Therefore, the CM generating system is expanded due to the introduction of tangential clamping forces at the output, generating 24 more variants of the new principles (table 2). For rotating objects, the total number of clamping principles will be 48 + 24 = 72. The next step to artificial intelligence in the search for new technical solutions is the use of wave and digital representation in the form of frequency pulses and binary code by analogy with the work [12], which is presented in Fig.9 in comparison with Fig.4.

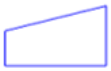
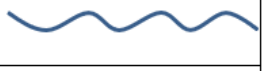
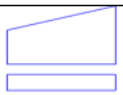
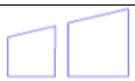
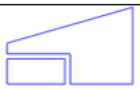
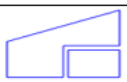
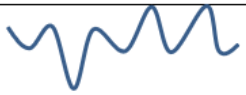
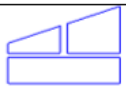
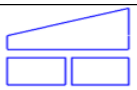
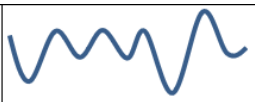
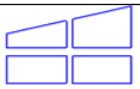
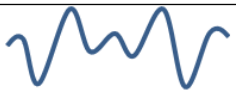
№	Structure	Geometric symbol	Binary code	Frequency pulse
1			0 0 0 0 0	
2			1 0 0 0 1	
3			0 1 0 1 0	
4			1 1 0 0 0	
5			1 0 0 1 0	
6			0 1 0 0 1	
7			0 0 0 1 1	
8			1 1 0 1 0	
9			0 1 0 1 1	
10			1 1 0 0 1	
11			1 0 0 1 1	
12			1 1 0 1 1	

Fig.9 *Binary codes and wave through frequency pulses for complete dissections of the wedge CE in XY plane action of force from the clamp drive*

The process of human-generator of ideas thinking can be represented as a combination of frequency pulse waves set with bursts of overcoming the psychological barrier and receiving feedback in memory and personal computer in the form of frequency pulses with the same parameters, within which resonant phenomena may occur, boosting the pulse (fig.10, 11).

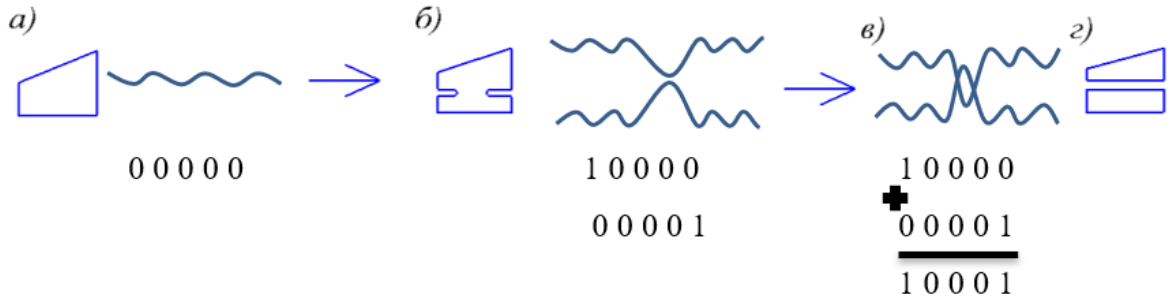


Fig. 10. *Transformation of technical solutions using wave representation through frequency pulses and binary code in the XY plane*

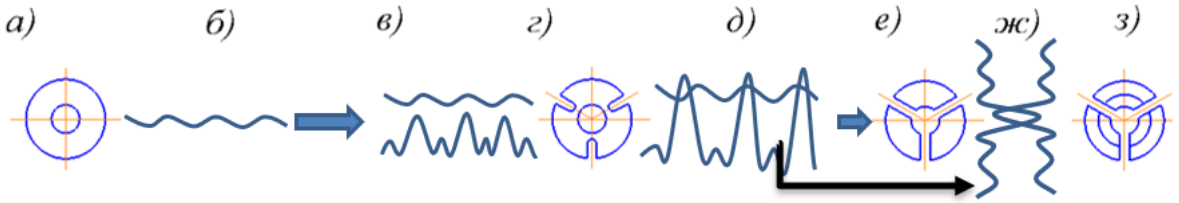


Fig. 11. *Transformation of technical solutions using wave representation through frequency pulses and their amplification in the XY plane*

Conclusion: The analysis of evolution stages for creative thinking with elements of artificial intelligence and the offered ideas and approaches allow asserting about the reality of simplified systems of artificial intelligence use the with a high level of creativity. Therefore, work in this direction must be continued.

References

1. Automation of search design (artificial intelligence in machine design) / A.I. Polovinkin, N.K. Bobkov, T. Ya. Bush and others .; under the editorship of A.I. Polovinkin. - M .: Radio and communications. - 344 p.
2. Balashov E.P.. Evolutionary Synthesis /E.P. Balashov – Moscow: Radio and Communications, 1985. – 328 p.
3. Bruhovich Ye.I. On the issue of society computerization. - //Mathematical Machines and Systems. – 1997, No. 2. – p.p. 122-132.
4. Bryukhovich E.I. Isomorphism in the evolutionary development of computer technology // Computerny zasobi, terezhi ta sistemi.-2005.-№4.-P.3-9.
5. Vavilov N.I.. Homologous series law in hereditary variation/N.I. Vavilov. – St. Petersburg: Science, 1987. – 267 p.
6. Vernadsky V.I.. Biosphere and noosphere /V.I. Vernadsky. – Moscow: Iris-press, 2007. – 576 p.
7. Ishlinsky A.Yu. Mechanics: nden, tasks, applications.-M .: Nauka, 1985.-624s.
8. Kuznetsov Yu. N. Challenges of the fourth industrial revolution "Industry 4.0" to the scientists of Ukraine // Bulletin of HNTU. No. 2 (61), 2017. - p.p. 67 - 75.
9. Kuznetsov Yu. N. A new look at the material point as a carrier of genetic information when creating technical systems // Materials of the International scientific-practical conference "Fundamentals of Mechanics", Novokuznetsk: SIC MS, 2016. - No 1.- p.p. 26-40.
10. Kuznetsov Yu. N., El-Dahabi F.W. The development of the genetic-morphological approach in the synthesis of machine tooling // Transactions of the International Scientific Conference UNITECH ”18, vol. 2, Gabrovo, 2018. – p..183-189.
11. Kuznetsov YM, El-Dahabi FV Directions for improving high-precision high-speed axisymmetric clamping mechanisms // Izvestiya KhNTU №46 (67), 2018.-P.70-75.
12. Nastasenko V.A., Nastasenko E.V. Artifical Intelligence Systems and possibility of Their Connection on with Creative Thinking Processes // Artifical Intelligence, N4, 2013. – p.p.28-36.
13. Nilson N. Artifical Intelligence Methods for finding solutions: transl. from English /N. Nilson. – M.: Mir, 1973. – 270 p.
14. Pigorov G.S., Creatology and intellectual technologies of innovative development / G.S. Pigorov, V.P. Kozinets, A.G. Makhmudov et al.-Dnepropetrovsk: Thresholds. 2003.-502 p.
15. Proydakov E.V., The current state of artificial intelligence,DOI: 10.31249/scis/2018.00.09.
16. Rassel Stuart, Norving Piter , Artificial Intelligence: A Modern Approach: Per. from English2006.-1408 p.
17. Self-adjusting clamping mechanisms: reference book / Yu.N. Kuznetsov, A.A. Vachev, S.P. Syarov, A.Y. Tsarvenkov; under the editorship of Yu.N. Kuznetsova.-K .: Technique; Sofia: State Publishing House "Technique", 1988.- 222 p.
18. Stankevich L.A. Artificial Intelligence and Artificial Intelligence in Robotics: Textbook. The allowance / L.A. Stankevich, E.I. Yurevich.-SPb .: Publishing house of the Polytechnic. University, 2012.-167 p.
19. Hamujela J.A. Gerra Genetic and morphological synthesis of clamping chucks: monograph / J.A. Gerra Hamuyela, Yu.N. Kuznetsov, T.O. Hamuyela; under the editorship of Yu.N. Kuznetsov. - Lutsk: Vezha-Druk, 2017 .- 328 p.
20. Shaumyan G.A. Automata and automatic lines.-M.: Mashgiz, 1961.-552 p.
21. Shinkarenko V.F., Fundamentals of the theory of evolution of electromechanical systems. - K .: Scientific Thought, 2002. - 288 p.
22. Schlesinger F.G. Metal cutting machines. M .: Mashgiz, 1936.
23. Yasnitsky L.N. Intelligent systems: a textbook. - M.: Knowledge Laboratory, 2016.-221 p.
24. Kelle Ph. Automaten, Spriger Verlag, 1951.
25. Zwicky F. Discovery, invention, research through the morphological approach /F.Zwicky.-Toronto; New York: MeMillan, 1969.

Stress-strain state of workpiece from Cu-Cr alloy processed by severe plastic deformation by ECAP

Ph.D. Eng. Asfandiyarov Rashid[1,2], Aksenov Denis[1,2], Dr. Eng. Raab Georgy[1]

Institute of Physics of Advanced Materials, Ufa State Aviation Technical University, Ufa, Russia [1]

Institute of Molecule and Crystal Physics, Subdivision of the Ufa Federal Research Centre of the Russian Academy of Sciences, Ufa, Russia[2]

Email: a.r.n@list.ru, aksyonovda@mail.ru, giraab@mail.ru

1. Introduction

The aim of this work is to study the stress-strain state and thermal effect in a workpiece from low-alloyed Cu-0.6Cr bronze under conditions of intense plastic deformation by equal-channel angular pressing (ECAP). To do this, physical modeling of the sedimentation of the samples was carried out on a Gleeble 3500 installation at temperatures of 20, 400, and 800 ° C and strain rates of 3, 30, and 300 mm / s. Based on the data obtained, a computer simulation of the process of ECAP was carried out in the Deform 3D software package. As a result, the fields of stress distribution, deformation, temperature (deformation heating) and power characteristics of the ECAP process are obtained, depending on various initial temperature and speed conditions.

2. Objective and research methodologies

The work used an industrial conductive alloy Cu-0.6Cr. The initial state was obtained in the process of high-temperature treatment at 1000 ° C for 1 hour and subsequent quenching in water. Alloy samples 10 mm in diameter and 14 mm in height were upset on a Gleeble-3500 physical modeling complex at a strain rate of 3, 30, and 300 mm / s. The temperature of the experiment was 20, 400, and 800 ° C. Further, based on the data obtained by physical modeling, a database was prepared for finite element computer modeling in the Deform 3D software package. After preparation, modeling and analysis of the results were carried out.

3. Results

Under conditions of severe plastic deformation by the ECAP method, intense deformation heating occurs (Figures 1,2). The deformation rate has the most significant effect on heating, so at an initial temperature of 400 ° C, with an increase in the deformation rate from 3 to 300 mm / s, deformation heating increases from 30 to 220 ° C.

With an increase in the initial temperature, the degree of heating decreases. So, at an initial temperature of 20 ° C and a deformation rate of 30 mm / s, the heating is 100 ° C, and at an initial temperature of 800 ° C, the heating is 30 ° C.

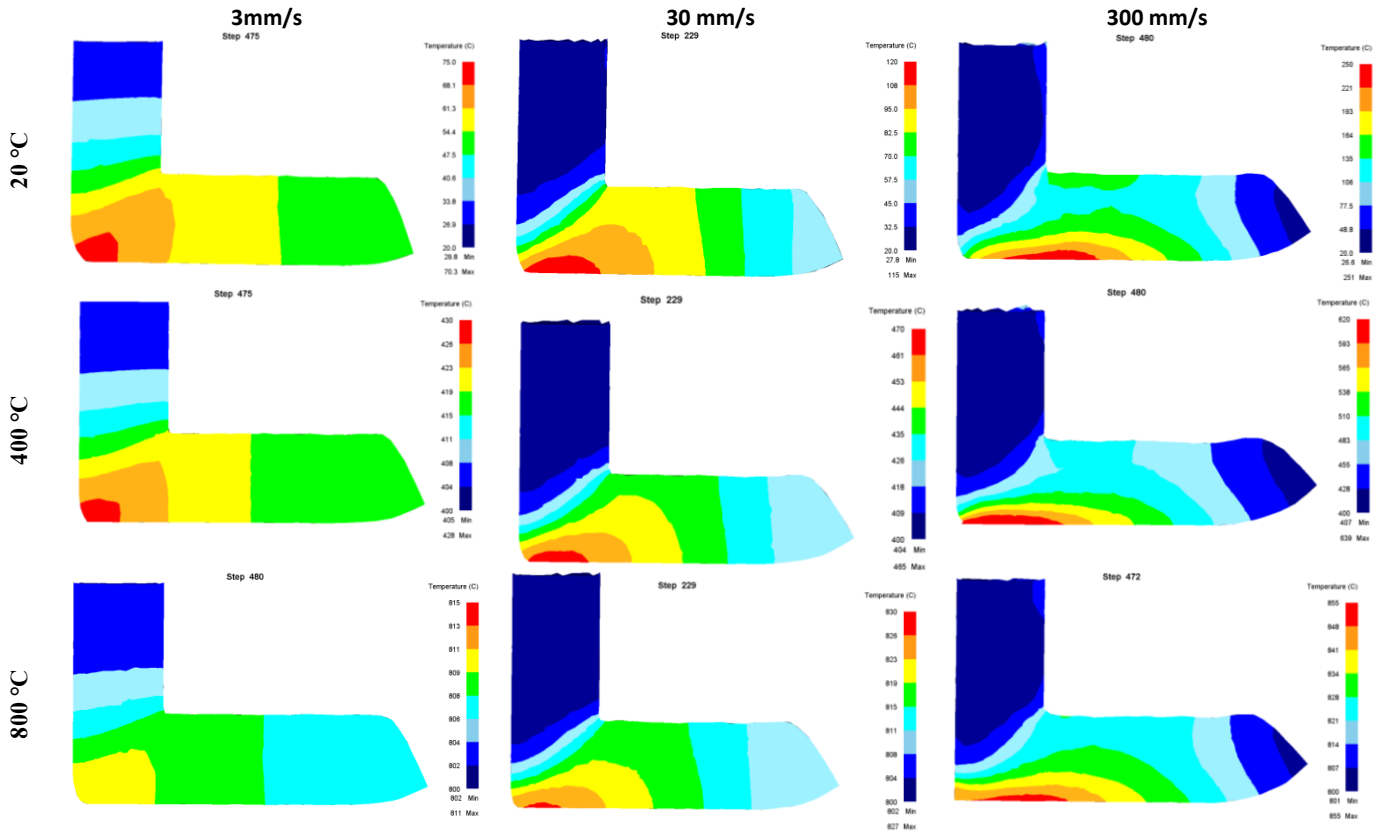


Fig. 1. *Temperature fields at different temperature-speed conditions*

With an increase in the initial temperature, the required pressing force (Figure 2) decreases, for example, from 208 kN at 20 ° C and a deformation rate of 3 mm / s to 46.3 kN at 800 ° C. An increase in the rate of deformation leads to an increase in the required force. For example, for 400 ° C, an increase in the deformation rate from 3 to 300 mm / s leads to an increase in the force from 113 to 244 kN. Thus, in the selected range of conditions, the most favorable is the mode including processing at an initial temperature of 400 ° C and a strain rate of 30 mm / s, providing a temperature increase of no more than 70 ° C and a low pressing force. The distribution of accumulated deformation (figure 3) is non-uniform. The maximum values are observed in the lower peripheral region and are e ~ 2.5, which can have a positive effect on the strength and wear resistance characteristics of the finished product. The minimum values in the central region are of the order of e ~ 1.5.

The simulation results show that in the deformation zone in the shear region, compression stresses prevail, reaching values of the order of 230 MPa. (Figure 4). In general, effective stresses in the deformation zone have a uniform distribution (~ 300 MPa) with local maxima in the peripheral zones of intersection of channels (more than 350 MPa). (Figure 5).

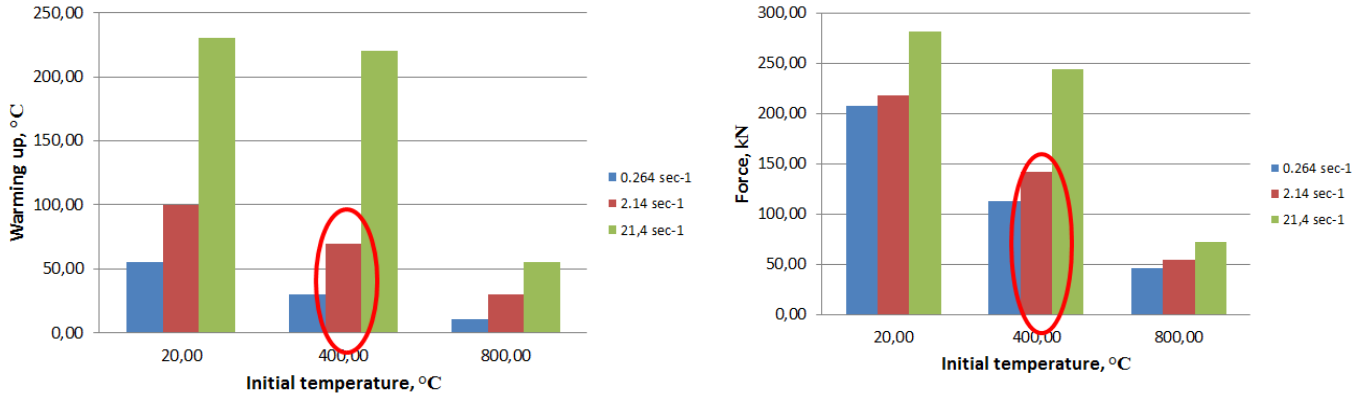


Fig. 2. *Variation of warming up during deformation and pressing force depending on the initial temperature and velocity*

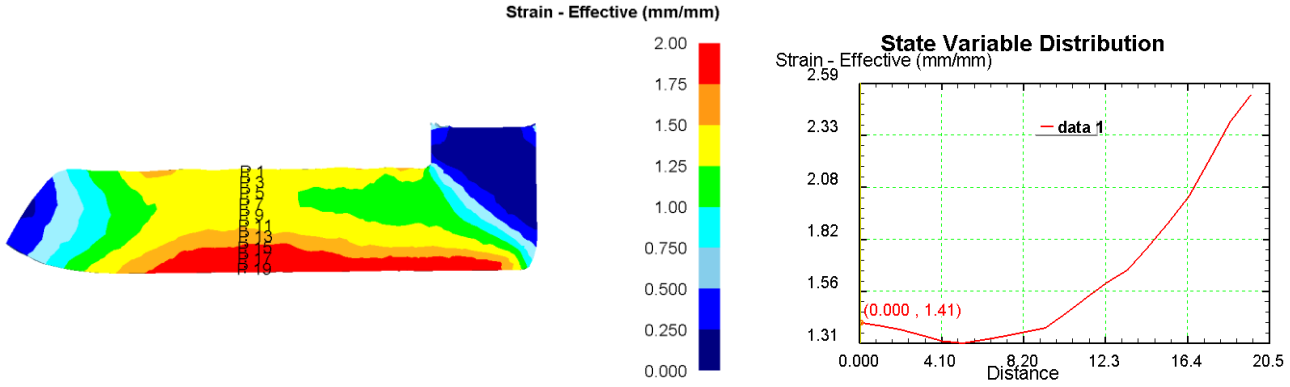


Fig. 3. *Accumulated deformation distribution (The rational technological mode)*

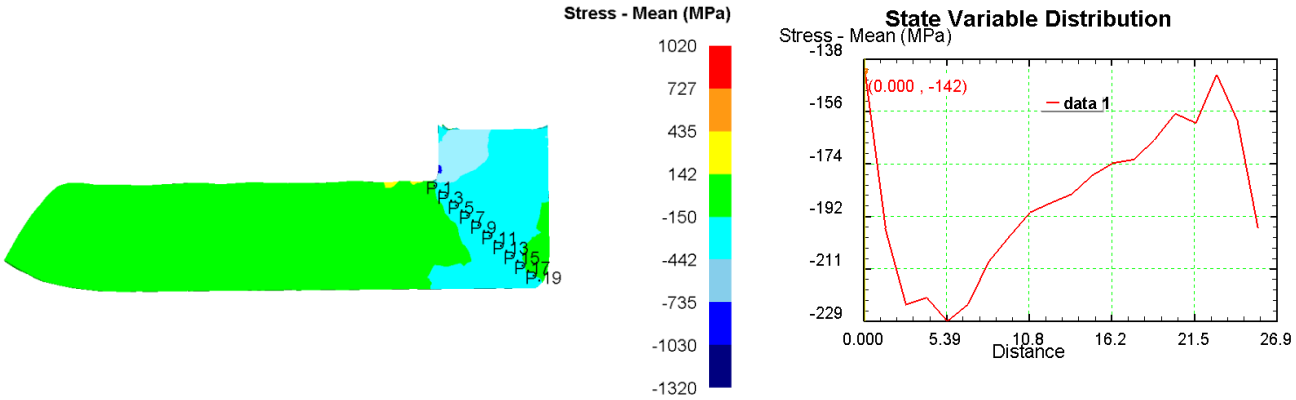


Fig. 4*. Stress mean distribution (The rational technological mode)*

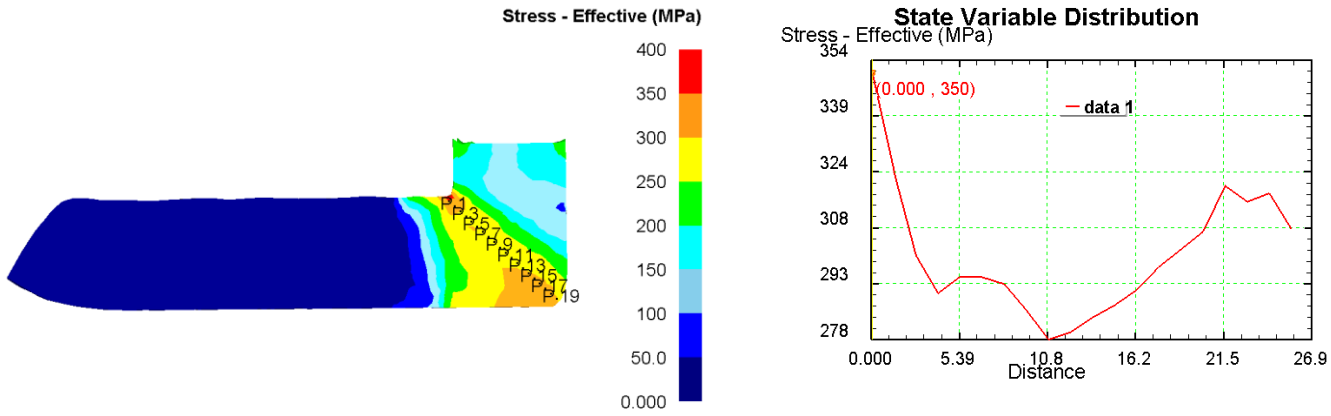


***Fig. 5**. Stress effective distribution (The rational technological mode)*

3. Conclusion

Thus, in the course of computer modeling, a comprehensive analysis of the stress-strain state of workpieces was carried out during processing by the ECAP method and ECAP with extrusion, an assessment of the energy-force models of the process, shown on the tool, was carried out, depending on the temperature and speed parameters of processing.

In conditions of intense plastic deformation by the ECAP method, intense warming up during deformation. The most significant effect on heating is exerted by the deformation rate, so at an initial temperature of 400 °C, an increase in the rate of deformation from 0.264 to 21.4 sec-1, deformation heating increases from 120 to 250 °C;

With an increase in the initial temperature, the degree of warming up decreases. So, at an initial temperature of 20 °C and a strain rate of 2.14 sec-1, the heating is 100 °C, and at an initial temperature of 800 °C, the heating is 30 °C;

With an increase in the initial temperature, the required pressing force substantially decreases, for example, from 208 kN at 20 °C and a strain rate of 0.264 sec-1 to 46.3 kN at 800 °C. An increase in the strain rate leads to an increase in the required force. For example, at 400 ° C, an increase in the strain rate from 0.264 to 21.4 sec-1 leads to an increase in force from 113 to 244 kN.

The optimal technological mode for the formation UFG structures is an initial temperature of 400 degrees and a strain rate of 2.14 sec-1 (equipment rate of 30 mm/sec) and true strain e~1.

Acknowledgments

The study was supported by the Russian Science Foundation (project №19-19-00432).

Remote real-time control of autoclave sterilization process

Stoyanka Madzharova[1,*], Rosen Gerasimov [2], Adriana Prodanova[3], Hristo Dinkov[1]
University of Food Technologies - Plovdiv, Bulgaria[1]
PU "Paisii Hilendarski"- Plovdiv, Bulgaria[2]
Technical University Plovdiv, Bulgaria[3]
nitani@abv.bg

Abstract: *The article proposes a variant for real-time sterilization process control from anywhere in the world, based on the widespread communication protocol RS-232 or RS-485.*
Keywords*: STERILIZATION, REAL-TIME CONTROL, DTE, DCE, COMMUNICATION PROTOCOLS*

1. Introduction

Sterilization remains one of the most widely used methods for preserving food. The correct conduct of sterilization regimes is an important stage in the technological process, which guarantees the production of food with high quality and a high level of microbiological stability.

Sterilization is a dynamic process (time-temperature dependent) and the creation of ideal or optimal conditions for its course is complicated. The process is a complex interaction between many interrelated factors that are difficult to reconcile with each other.

The challenge for the canning industry is to reduce costs - the presence of microflora in cans under the established sterilization regime is one of the reasons for marriage and leads to increased costs. In a certain sterilization regime in a certain autoclave there is a dependence between the development of thermal processes in it and in canned food. It finds expression in the so-called sterilization formula. For devices with periodic action, in which each sterilization cycle begins with a program, the conditional record is:

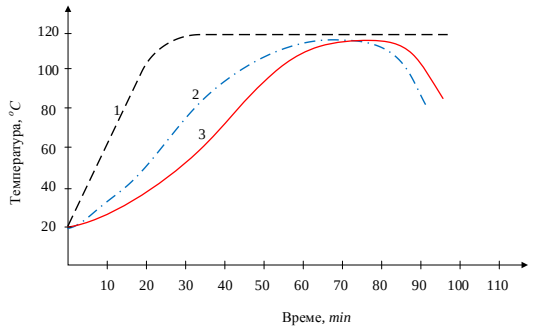
$$\frac{A+B+C}{t^0} \qquad (1)$$

where: *A* - duration of temperature rise in the autoclave from the initial to the set temperature, min;

B - Duration of temperature retention at the set level, min

C - Duration of lowering the temperature to the set temperature, min

t ^{0} - sterilization temperature, the maximum temperature of the heating medium, $^\circ$C.



1 - топлоносител, 2 - течната част в консервата, 3 - плътната част в центъра на

Fig. 1 *Кривите на температурни промени във времето*

The temperature change curve is directly related to the temperature curve of the medium of the heat carrier (autoclave).

On the basis of mathematical models, sterilization methods have been created, based on the correct choice of temperature and time for the most difficult heating point in the can, depending on the type of microorganism that will be inactivated.

2. Materials for Production of Prototype Parts

Often the objects for research, control and management are characterized by a large number of various physical parameters that need to be transformed and measured. The incoming measurement information from the transducers is collected, processed and presented to the operator in an appropriate form. Some of the information needs to be responded to immediately, and the rest is recorded and further processed. Then it is necessary to build information and measurement systems. / The term "distributed *metering systems" or "data collection systems"* is also used /.

In the most general case, the information-measuring system is a complex measuring instrument, composed of measuring transducers, measures, devices and switches, connecting lines, digital and analog computing devices, designed for automated receipt of data from the studied object, for processing measuring information. and for converting the data into output signals of the system [1].

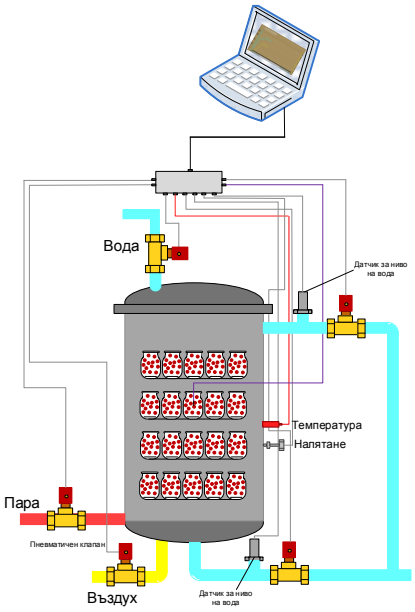


Fig. 2*. Вертикален периодичен автоклав с управление*

The management of the sterilization process must ensure the production of a safe and quality product, without deformations on the packaging. The control can be manual by operator, semi-automatic and fully automatic. In fully automatic control much of the currently used autoclaves in the canning industry, are adapted to communicate with the computer uses Aiki this communication protocols RS-232 or RS-485.

In telecommunications, RS-232 is a standard originally introduced in 1960 [2] for the transmission of serial data communications. It formally defines signals connecting the DTE (data terminal equipment) as a computer terminal and the DCE (data circuit termination equipment or data communication equipment) as a modem. The standard specifies the electrical characteristics and timing of the signals, the meaning of the signals, as well as the physical size and pins of the connectors. The current version of the standard is the TIA-232-F interface between data terminal equipment and data end-use equipment using serial binary data exchange, issued in 1997. The RS-232 standard is commonly used in computer serial ports and it is still widely used in industrial communication devices.

A RS-232-compliant serial port was once a standard feature on most types of computers. Personal computers have used them to connect not only to modems, but also to printers, computer mice, storage, uninterruptible power supplies, and other peripherals.

RS-232, compared to later interfaces such as RS-422, RS-485 and Ethernet, has a lower transmission speed, short maximum cable length, large voltage swing, large standard connectors, no multipoint capability and limited multidrop ability. In modern personal computers, USB has displaced the RS-232 from most of its peripheral interface roles. Few computers today are equipped with RS-232 ports, so one must use either an external USB to RS-232 converter or an internal expansion card with one or more serial ports to connect to RS-232 peripherals. . Nevertheless, due to their simplicity and ubiquity, RS-232 interfaces are still used - especially in industrial machines, network equipment and scientific instruments, where low-speed point-to-point and low-speed cable connections are perfectly adequate.

The short cable length is one of the serious limitations of the protocol. By default, the maximum cable length is 50 feet (15.24 meters) or the cable length is equal to a capacity of 2500 pF.

This limitation is often a serious problem in working with industrial machines using RS-232 or RS-485 protocols for communication. In FIG. 3 shows a variant for real-time communication.

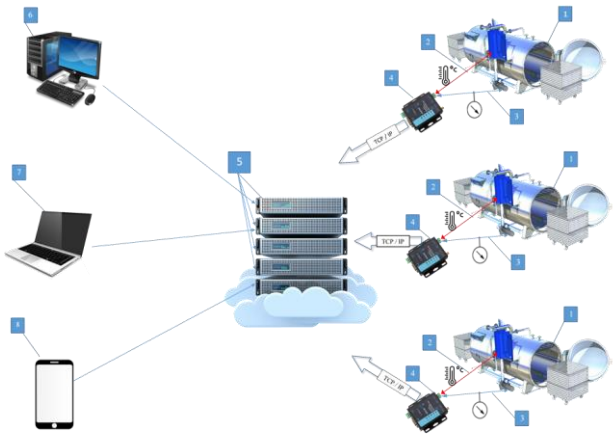


Fig.3 Real-time communication scheme

In *position 1* are denoted autoclaves, located at different places (proceedings), no matter how geographically remote from one another. Autoclaves can perform different sterilization processes with different products, as well as be owned by different canning companies.

With *the 2-position* are indicated, and temperature sensor corresponding thereto interface cable.

With *position 3* - pressure sensor and the corresponding interface cable.

With *Position 4* - industrial converter RS232 / RS485 to TCP / IP, with models only with LAN port, and there are also models with the possibility of Wi-Fi connectivity (according to the 802.11 b / g / n standard). Even when using the combined model converter recommend is connect to the LAN port of the converter recommended cable - FTP category 5. This type of cable has an overall shield of foil wrapped around not shielded twisted pairs and drain wire. When the drain wire is properly connected, unwanted noise is diverted to ground, offering additional protection against electromagnetic interference (EMI) or radio frequency interference (RFI).

With *Items 6, 7 and 8* are depicted different types of devices (PC, laptop, tablet or smart phone), which could not access real-time information available to group virtual machines (*Item 5*) .

Item 5 can be a physical computer (server) or group (virtual) machines, part of a private or public cloud , for example . : Amazon Elastic Compute Cloud (EC2), Windows Azure and others. The use of virtual machines will reduce LSI mended chance of data loss and and reduces the cost of owning and maintaining the necessary information infrastructure. The use of virtualization in the present case it will allow and to significantly reduce the cost of license fees for the necessary software .

The proposed technical solution can be applied successfully not only in KONS ervnata industry as it is in the specific example, but in many other manufacturing processes. For example: CNC machines, medical equipment and others. Many industries use various (expensive) equipment that is designed to use RS-223 as a communication and control protocol.

Overcoming the above-mentioned limitations of RS-232 in combination with our proposed use of virtual machines with remote access (*Position 5*) will allow the use of highly specialized and expensive software for control of the respective machines of the **SaaS** or **IaaS** model .

Cloud computing is computing services provided to a user via a remote computer to which the user connects via the Internet or a dedicated communication line.

The term combines concepts such as software as a service (*software as a service*, **SaaS**), infrastructure as a service (infrastructure as a service, **IaaS**), platform as a service (*platform as a service* , **PaaS**) and other modern technologies in the form of online business web browser applications meet computing needs while storing software and user data on their servers.

In other words, the term refers both to software applications provided in the form of web services and to access to the hardware and system resources of the data center that offer these services. In fact, the combination of access to the center's hardware and software is what is commonly called a cloud. The cloud is considered a metaphor for the Internet, as it is often depicted in computer network diagrams and as an abstraction of the complex infrastructure behind it. [3]

Infrastructure as a Service (IaaS) is a cloud based system of hardware and software , in which the provider and provides users with access to computing resources such as servers, storage of their data and networking. Customers (*item 1*) use their own platforms and applications within the service provider's infrastructure [4] . Main advantages of **IaaS** :

Instead of buying watt hardware directly, the user pays for IaaS as needed .

The infrastructure is scalable depending on the processing and storage needs.

Saves companies the cost of purchasing and maintaining their own hardware.

Because the data is in the cloud, there can be no point of failure.

Allows the virtualization of administrative tasks, freeing up time for other work.

Software as a Service (SaaS) is a cloud- based service that offers users access to a provider's cloud software. Users do not install applications on their local devices. Instead, applications reside on a remote cloud network that is accessed by the network or API. Through the application, users can store and analyze data and collaborate on projects. [4]

Main advantages of **SaaS** :

Providers of **SaaS** services provide goods - applicants the necessary hardware, infrastructure, software and software (applications) via a subscription model.

Users must not manage, install or upgrade software; SaaS vendors manage this.

Data is protected in the cloud; equipment damage does not result in data loss.

Resource usage can be reduced depending on the needs of the service.

The applications are accessible from almost any device connected to the Internet, from almost anywhere in the world (*Positions 6, 7 and 8)* of Fig.3 .

Both of the above models (**IaaS** , **SaaS**) of use are well applicable and "fit" to solve the problem addressed in our report . Users with more specific needs , as well as their own IT professionals, would be better to choose **IaaS** , it will give them more freedom to use, but also requires higher own IT expertise. Users who do not have very specific needs when using the software or do not have their own IT experts should choose the **SaaS** usage model .

In recent years, there are many examples of the use of the SaaS model , most of the major IT companies such as Google, Cisco, Microsoft , DropBox and many others . Microsoft Office 365 is one example of a SaaS product that most of us know and have used.

The **SaaS** usage model is a kind of peak in the development of virtualization in recent years and gives a significant competitive advantage to companies that put it to use in the management of their production and business processes.

Why companies perceive Sass ?

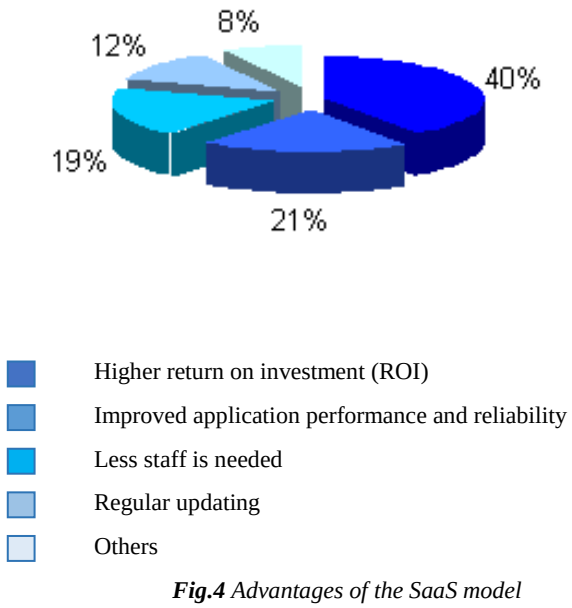


Fig.4 *Advantages of the SaaS model*

Fig.4 graphically presents the main advantages that users find in the SaaS usage model . [5]

In a particular case, each owner of an autoclave or group of autoclaves (*item 1*) will not need to own and configure a server and the necessary specialized software. It will use a virtual machine, part of (*item 5)* with the necessary monitoring and control software installed on it . This significantly reduces the implementation time and the complexity of the process of modernization of the production process of sterilization.

The interesting question is what type of users would need the information so aggregated so far?

Possible users are:

1. Technologists monitoring and responsible for the relevant sterilization processes. These specialists could be, as well as employees of the company, the owner of the autoclave, and external experts hired to control the process.

2. Customers (with high quality requirements) of the respective canning production, who could observe (themselves or their specialists), the process of sterilization of the ordered (and we assume paid) production.

3. Students and lecturers from higher education institutions (UFT, etc.) with specialties related to training for the canning industry.

These three groups of users will be able to monitor and control the actual sterilization production processes from anywhere in the world. Something that was not possible with the existing restrictions imposed by the widespread use in industrial machines of the communication protocols RS 232 / RS 485. Any of the potential users could use to access any of the devices under *Positions 6, 7 and 8* .

3. Conclusions

1. Versatility of the proposed model for overcoming the limitations of the communication protocols RS 232 / RS 485 widely used in equipment and machines

2. Enabling remote Internet access to industrial equipment and machinery using RS 232 / RS 485, protocols operating at short distances

3. Applying of the SaaS (Software As A Service) model for the use of software for a large group of software products managing industrial processes. A fact that leads to increasing the competitiveness of existing industries.

4. References

1. Модули за обработка на сигнали от сензори //Списание “Инженеринг ревю”, декември, брой 9, 2011. [Online]. [cited 12.07.2015]. Available from: http://engineering-review.bg/engineering-statii.aspx?br=74&rub=803&id=1837/.M. Ben Rabha, M.F. Boujmil, M. Saadoun, B. Bessaïs, Eur. Phys. J. Appl. Phys. (to be published)
2. Evans, Jr., John M.; O'Neill, Joseph T.; Little, John L.; Albus, James S.; Barbera, Anthony J.; Fife, Dennis W.; Fong, Elizabeth N.; Gilsinn, David E.; Holberton, Frances E.; Lucas, Brian G.; Lyon, Gordon E.; Marron, Beatrice A. S.; Neumann, Albercht J.; Vickers, Mabel V.; Walker, Justin C. (October 1976), Standards for Computer Aided Manufacturing F. De Lillo, F. Cecconi, G. Lacorata, A. Vulpiani, EPL, **84** (2008)
3. https://bg.wikipedia.org/wiki/%D0%98%D0%B7%D1%87%D0%B8%D1%81%D0%BB%D0%B5%D0%BD%D0%B8%D1%8F_%D0%B2_%D0%BE%D0%B1%D0%BB%D0%B0%D0%BA , 30.06.2020
4. https://www.ibm.com/cloud/learn/iaas-paas-saas, 30.06.2020
5. https://cio.bg/management/2009/07/14/3449654_modelut_softuer_k ato_usluga_vuprosi_i_otgovori/, 30.06.2020

Model for high-pressure water atomization of metal melt using a vortex type jet

Ternovoy Yu.[1], Bagliuk G.[2], Panova V.[1]

Institute of Engineering of the National University, Zaporizhzhia, Ukraine[1]
Institute for problems of materials science, National Academy of Science of Ukraine, Kyiv, Ukraine[2]
gbag@ukr.net

Abstract: *In this paper the physical model for high pressure water atomization of metal melts using hydraulic nozzle of a vortex type was proposed. The developed model assumes, that due to high speed water flow with significant centrifugal component of its velocity vector the rarefaction is formed, which causes intensive air suction leading to the formation of rotating gas (vapor-air) layer of toroid-like shape, providing a gap between the water flow and the metal stream. Thus water stream is separated from the heated surface of metal stream and the formation of particles during crystallization of melt droplets occurs due to surface tension mainly in this vapor-air layer. The cooling of melt droplets in the gas-water leads to the formation of spherical powder particles. The proposed model correlates well with the known experimental data on the production of spherical powders using a vortex-type annular hydraulic nozzle.*

Keywords: *model, metal powder, water atomization, nozzle, melt, jet, swirling, crystallization, gas ejection, particles.*

1. Introduction

One of the most common methods for producing of metal powders in large-scale production is water atomization of the melt [1]. The process of water atomization of liquid metal with using of a ring nozzle according to the standard scheme has been widely studied experimentally and theoretically [1-3]. When using this technology in a wide range of technological parameters of the process, the powder particles acquire an irregular shape, which partially limits their scope, in particular due to the relatively low yield.

As a result of a change in a number of basic parameters of the atomization process, namely, the angle of attack of the water flow causing it to "twist", the authors [4] and later [5] proposed and experimentally substantiated a method for producing powders whose quality is fundamentally different from that characteristic for traditional water atomization schemes.

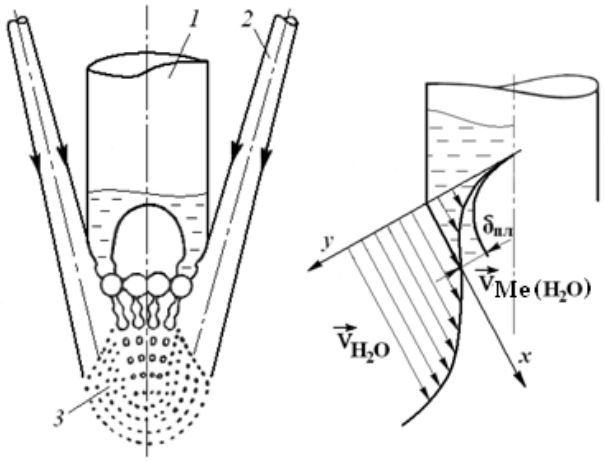
This method was the basis of technologies that received the name, respectively, "atomization of melts with high-pressure water in air-water whirlwing" or «ultra high pressure swirl water atomization».

In [6] we showed that the atomization of melts with high-pressure water in whirlwing conditions is a promising scheme for the production of metal powders with increased bulk density and fluidity up to the production of spherical powders. At the same time, if the theoretical foundations of processes are sufficiently deeply developed for traditional schemes for melts water and gas atomization, and atomization using centrifugal forces, then information on the particle formation mechanism for the scheme for atomization of melts with water "in whirlwing conditions" is practically absent in available literature sources.

Thereby, the aim of the present work was to analyze the known experimental data and develop a schematic model of the mechanism of formation of powder particles using a melt atomization scheme that ensures the formation of a rotation of the water flow in the nozzle area.

2. Research results and discussion

In [2] the model of the process of atomization the melt with high pressure water [2] was presented, which was tested for the manufacturing of high speed steels, ferroalloys, complex alloys, aluminum alloys powders. The model includes the following steps (fig. 1): transformation of the initial metal stream upon contact with the water stream into a conical film converging to the axis of the stream; development of longitudinal and transverse waves on the film surface; instability and decay of the end of the film into droplets. Drops of metal are intensively cooled in the spray zone in a water-vapor medium and crystallize quickly without reaching geometric equilibrium in the form of coral-shaped particles (fig. 2).



a *b*

Fig. 1. *Model scheme for atomization of liquid metal jet (a) and velocity distribution in a water-metal system (b):*
1 - stream of metal; 2 - annular flow of water; 3 - cooling zone of metal droplets;V_{H2O} - water flow speed; $V_{Me\ (H2O)}$ - speed of metal stream; δ_{pl} - metal film thickness

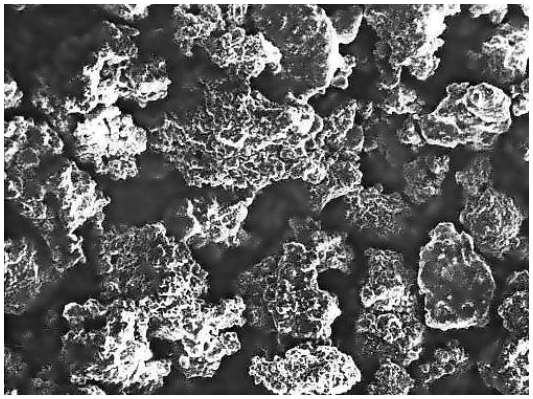


Fig. 2. *Coral-shaped particles of 50Mn-12Si-17Ni-9Fe powder*

The formation of coral-like particles is caused by the action of dynamic water flow, as well as by the boiling of water droplets formed when water enters the melt, which confirms the structure of the surface layer of the crystallized plume section in the atomization unit (fig. 3).

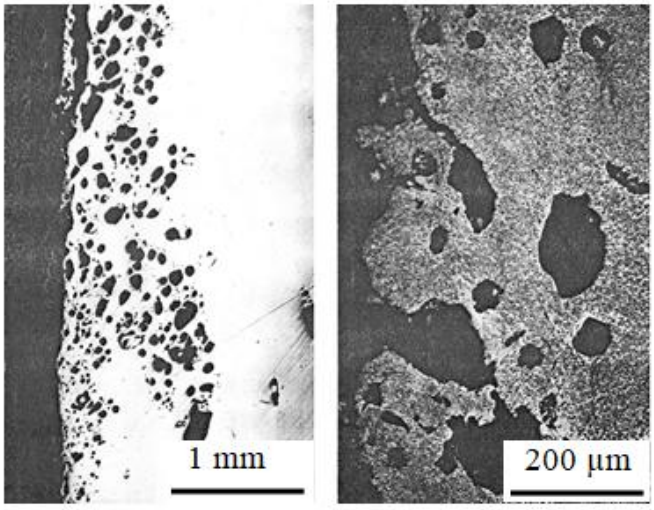


Fig. 3. *Macro (a) and microstructure (b) of the subsurface layer of crystallized section of melt jet flame for water atomization of P6M5 high speed steel*

As it had been shown by the results of theoretical and experimental studies of the traditional process of water atomization, with an increase in water consumption, its flow rate and the temperature of the melt overheating, which contributes to a decrease in its viscosity, the likelihood of obtaining finer powders at a given thickness of the metal jet increases. However, it is not possible to affect the particle shape of the main powder fraction during atomization according to this mode.

Unlike the traditional water atomization process, the feature of "tornado" atomization technology in the is the atomization of liquid metal jet of a vortex-type annular hydraulic nozzle (fig. 4,a), which supplies a high-pressure water jet along its axis while rotating it around metal stream. This character of the jet flow is ensured by the set of the nozzle's special design, which provides for a change in the direction of the axes of the nosepieces in such way that the horizontal component of the water jet velocity vector in each nozzle is directed at an angle $\omega>0$ relative to the radial direction (fig. 4,b).

The rotational movement of the water stream causes the formation of the centrifugal component of the velocity vector of its movement, which leads to the formation of rotating water stream in the form of a hyperboloid (fig. 4,c), into the cavity of which a metal stream is fed.

Moreover, while using traditional methods for producing powder by high-pressure water atomization of the melt, the powder particles have a predominantly coral-like shape (fig. 5,a), the use of a ring nozzle with rotating jet results in powder particles of a spherical or spheroidal shape (fig. 5,b).

The results of experimental studies of real processes of melts atomization using of hydraulic nozzle of a vortex type with application of high-speed filming made it possible to propose a physical model of atomization in the following mode.

When a water jet contacts a surface of melt jet heated by more than 550-600 °C, the so-called film boiling occurs, when water is separated from the heated surface by a continuous film - vapor shell. Moreover, in the area of the neck of the hyperboloid (fig. 5,c) and below, due to the presence of significant centrifugal component of the water flow velocity vector, the rarefaction is formed, which causes intensive air suction leading to the formation of rotating gas (vapor-air) layer, providing a gap between the water flow and the metal stream of order of thickness of about 10^{-3} m (fig. 6).

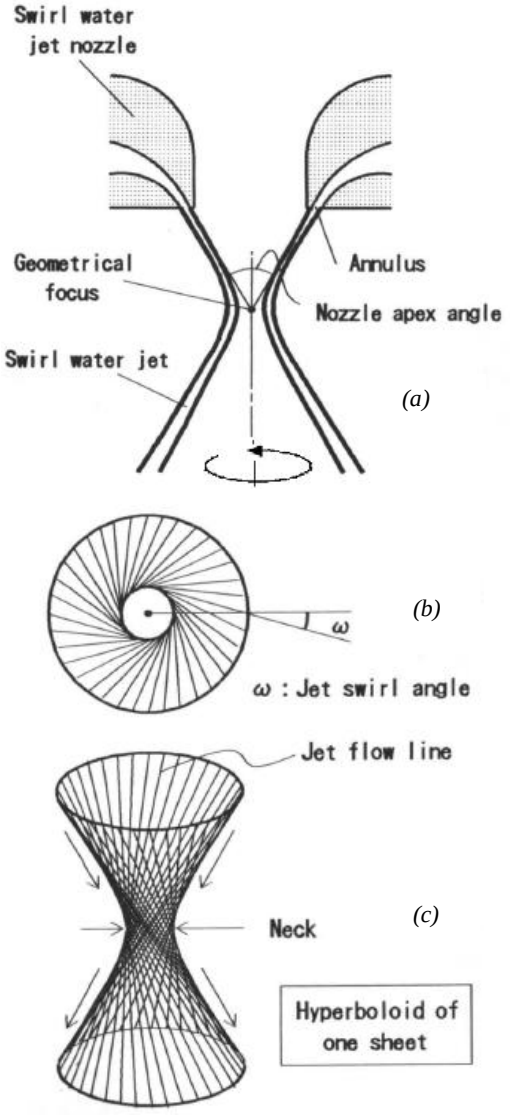


Fig. 4. *Schematic cross-section of water jet for water atomization in air-water whirlwing (a) and schematic diagram of air-water stream (b, c) [7]*

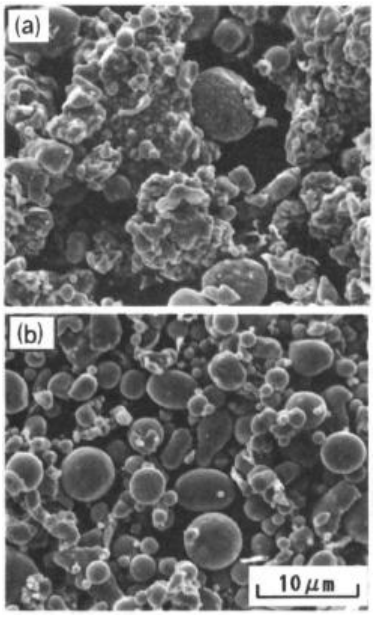


Fig. 5. *SEM micrographs of Cu-10 % Sn alloy powders produced by high-pressure water atomization using traditional technology (a) and ring nozzle with rotating jet (b) [7]*

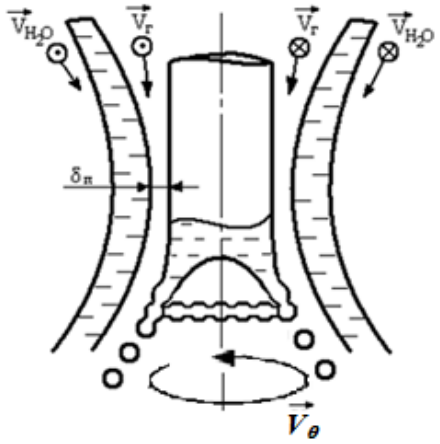


Fig. 6. *Flow separation scheme for atomization using a vortex type nozzle:V_{H2O} - velocity of the water conical stream; $V_г$ - velocity of the ejected gas (air); $\delta_п$ - the gap between the water and the jet of melt; V_θ - circular rotation velocity of the air-water stream*

Under the influence of gas-dynamic vacuum generated in the region of the vapor-air layer, the initial cylindrical stream of liquid metal is deformed: a hollow liquid-metal cone is formed from it, thinned in its lower part to the film-like thickness. At the same time, oscillatory processes develop in a thinning melt film due to the instability of its motion as a result of small-order disturbances. Roughnesses and roughness of the nozzle surface, irregular hole geometry, pulsations in the liquid, etc. can serve as a source of the latter. Initial perturbations favor the formation of waves, which, in turn, increase, first contribute to the formation of a liquid toroidal thickening along the periphery of the film, and then to pinch the jet and separate it into separate strands - melt micro-jets flowing from the periphery of the film. The latter, in turn, under the influence of disturbing forces break up into droplets.

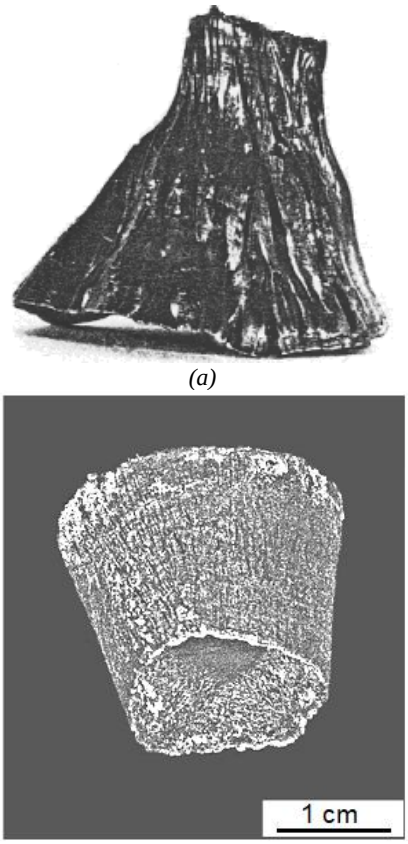
The spherical shape of the obtained powder particles in this case is explained by the fact that the formation of particles during crystallization of the melt drops occurs mainly due to surface tension in the vapor-air layer, when the rotating stream of water from the nozzle does not touch the metal stream but only the final solidification and cooling of the powder particles occurs in water.

Such a cooling regime significantly changes the thermophysical characteristics of the process compared to conventional methods of water atomization, since the vapor-air layer, due to the reduced heat transfer coefficient, removes heat much worse than water, which leads to a significant decrease in the crystallization rate.

In addition, due to the rotational component of the flow rate and the absence of direct contact of the melt jet with water, the particles collide less with each other and experience less deforming effect on their shape.

The speed of the gas column is determined by the flow rate of water V_{H2O} (fig. 6) and significantly decreases with distance from the surface of their contact. Therefore, the thickness of the gas layer $\delta_п$ is of great importance, which is ensured by a combination of the geometric parameters of the nozzle for the diameter of the metal jet. To ensure effective atomization, it is necessary to achieve some optimal (minimum) value of $\delta_п$, at which the gas flow rate will correspond to the velocities characteristic of gas atomization. The angle of attack of the water flow, as well as the angle of its swirling, are in this case those parameters that determine the location and depth of the created vacuum, and therefore the magnitude of the ejection and the flow rate of the sucked gas.

The indirect confirmation of the adequacy of the proposed model is the appearance of the crystallized section of the torch of the melt jet, which remains after the completion of the atomization process using a vortex-type nozzle (fig. 7, a), which differs significantly from the similar portion of the torch obtained using a direct-flow nozzle (fig. 7, b).

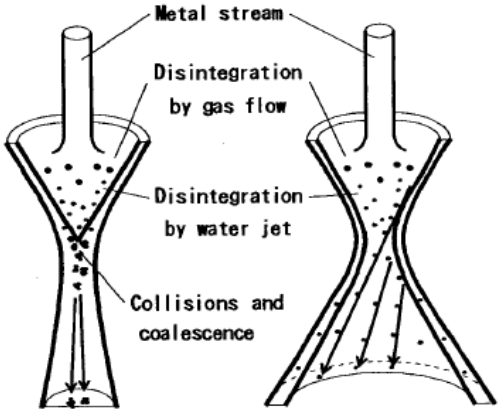


(a)

(b)

Fig. 7. *Crystallized section of melt jet flame for atomization using a vortex-type nozzle (a) and with using of a direct-flow nozzle (b)*

The results presented on fig. 7 also correlate well with the model of water atomization in a vortex flow proposed in [7], which is conditionally displayed in fig. 8.



(a) *(b)*

Fig. 8. *Models of high-pressure water atomization using a direct-flow nozzle (a) and a vortex-type nozzle [7]*

Thus, the proposed model allows us to conclude that atomization under the conditions of vortex motion of an energy carrier jet is essentially gas-like atomization with gas moving at a speed and in the direction determined by the flow of water, which also determines the temperature gradient of the gas layer.

However, the analysis of the microstructure of powder particles obtained using this technology indicates substantially cellular nature of the structure (fig. 8), which indicates high crystallization rates, significantly exceeding the crystallization rates during traditional (water free) gas atomization. The reason for the noted effect is the

presence in the gaseous layer of significant amount of microscopic drops of water, which lead to quenching of the metal drops during their crystallization, which was shown earlier in [8].

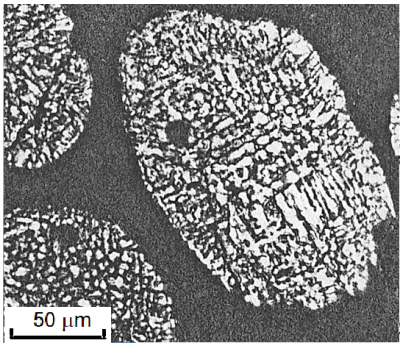


Fig. 8. *The microstructure of ferromanganese powder produced by water atomization using a vortex type nozzle*

3. Conclusions

1. Using of hydraulic nozzle of a vortex type for high-pressure water atomization of the melt provides spherical shape of powder particles.

2. The physical model of atomization using hydraulic nozzle of a vortex type was proposed. In accordance with this model, water stream is separated from the heated surface of metal stream with a continuous film - vapor shell and the formation of particles during crystallization of melt droplets occurs due to surface tension mainly in this vapor-air layer.

References

1. Nichiporenko O.S., Naida Yu..I., Medvedovsky L.B. Atomized metal powders. Kiev: Naukova Dumka. 237 p. (1980). (In Russian).

2. Ternovoi Yu.F., Bagliuk G.A., Kudievsky S.S. The theoretical basis of the processes of metal melts atomization. Zaporozhye: Publishing house of ZGIA. 298 p. (2008). (In Russian).

3. Handbook on non-ferrous metal powders: technologies and applications. Ed. Neikov O., Naboychenko S., Yefimov N.V. Elsevier. 974 p. (2019).

4. USSR certificate of authorship 1603649. A method of produsing of passivated powder of medium-carbon ferromanganese / UKRNIIspetsstal / Yu.F. Ternovoi, V.I. Bilan, A.P. Alexandrov / Publ. 10.27.89. (In Russian).

5. U.S. Patent US6336953 B1. Kikukawa M., Matsunaga Sh., Inaba T. et al. Method for preparing metal powder. (2002).

6. Ternovy Yu. F., Vodennikov S.A., Panova V.O. Producing powders of increased fluidity by atomization with high pressure water in a double air-water tornado. Metallurgy: ZDIA. Issue 2 (**40**). P. 33-37. (2018). (In Ukrainian).

7 . Kikukawa M., Matsunaga S., Inaba T., Iwatsu O., Takeda T. Development of Spherical Fine Powders by High-pressure Water Atomization Using Swirl Water Jet. Journal of the Japan Society of Powder and Powder Metallurgy Vol. 47 (**5**). P.453-457. (2000).

8. Ternovoy Yu.F., Panova V.O. Forced heat transfer and cooling rate of droplets when Atomization the melt with water. Metallurgy: ZNU. Issue 1 (**1**). P. 15-18. (2019). (In Russian).

Structure and properties of microarc oxide coatings on high-temperature aluminum alloy

Valeriia Subbotina, Oleg Sobol'

National Technical University «Kharkiv Polytechnic Institute», Kharkiv, Ukraine
E-mail: subbotina.valeri@gmail.com, sool@kpi.kharkov.ua

Abstract. *To create a high-hardness and wear-resistant coating on the heat-resistant aluminum AK4 alloy, the technology of microarc oxidation is used. The possibility of forming an oxide layer on the surface (mainly of $\alpha-Al_2O_3$ and $\gamma-Al_2O_3$ phases) with a thickness of about 150 μm and a hardness of 17000 – 18000 MPa is shown. For this, the process of microarc oxidation was carried out at a current density of 20 A/dm^2 in an electrolyte of the composition KOH (1-2 g/L) and Na_2SiO_3 (6-12 g/L). The obtained properties of MAO coatings on the AK4 alloy make it possible to effectively use such materials for engine elements.*

KEYWORDS: *AK4 ALUMINUM ALLOY, MICROARC OXIDATION, ROUGHNESS, COATING THICKNESS, PHASE COMPOSITION, MICROHARDNESS.*

1. Introduction

Aluminum alloys and aluminum occupy a significant place in modern technology as one of the most important materials. They are widely used for the manufacture of various parts and structural elements, when the leading role is played by low weight, high plasticity, corrosion resistance, and good weldability. It is possible to significantly expand the scope of application of aluminum alloys by applying various coatings to products. There are many known coating methods, such as gas, detonation, plasma, electrochemical, vacuum spraying and others. However, the method of microarc oxidation [1, 2] allows to obtain a fundamentally new quality of coatings. The method of microarc oxidation (MAO) is a technology that makes it possible to obtain a coating with a special spectrum of properties on valve metals [3]. This method makes it possible to form coatings on aluminum and aluminum alloys, which are thicker than traditional oxide films, firmly adhered to the base and have high mechanical, heat-resistant, wear-resistant, anticorrosive and antifriction properties [4].

It is especially important to form an oxide coating on heat-resistant aluminum alloys that are used in engine building. Such alloys include AK4 alloy (analogue of ENAW-2618A), which was developed for engine parts operating under conditions of external thermal and cavitation effects, and therefore requiring high hardness and wear resistance of surface layers.

To optimize the technology of obtaining MAO coatings on such alloys, specialized studies are required, which is the subject of this work.

In this regard, the aim of the research was to study the effect of the type and composition of the electrolyte on the kinetics of MAO coatings growth on the AK4 alloy, the formation of the phase-structural state of the coatings, and the effect of their phase composition on the hardness.

2. Materials and methods

Samples of AK4 aluminum alloy were subjected to MAO treatment (composition of the main elements: Al (91.2–94.6 %), Cu (1.9–2.5 %), Mg (1.4–1.8 %), Fe (0.8–1.3 %), Ni (0.8–1.3 %), Si (0.5–1.2 %) Samples had the shape of cylinders 30 mm in diameter and 10 mm high.

Microarc oxidation was carried out in a 100 liter bath. During the MAO process, cooling and bubbling of the electrolyte was provided [5]. The bathroom body served as a counter electrode. A 40 kW capacitor-type power supply was used. Oxidation was carried out in the anodic-cathodic mode. The average voltage was 380 V. The current density was 20-30 A/dm^2.

A mixture of a solution of caustic potassium (KOH) in distilled water and a solution of liquid glass (Na_2SiO_3) in distilled water was used as electrolytes. Preliminary studies have shown [6, 7] that the most technologically advanced compositions for processing aluminum alloys are:

1) 1 g/L KOH + 6 g/L Na_2SiO_3;
2) 2 g/L KOH + 12 g/L Na_2SiO_3.

The determination of the phase composition of MAO coatings was carried out according to the results of X-ray phase analysis. The studies were carried out on the DRON-3 diffractometer (Burevestnik, Russia) in monochromatic K_α–Cu radiation. For quantitative phase analysis, the method of method of standard mixtures was used [8].

The coating thickness was determined using a VT-10 NTs vortex thickness gauge. The error in measuring the coating thickness is no more than 5 % at the smallest coating thickness (about 10 μm).

Microhardness was determined using a PMT-3 device.

To study the surface morphology and determine the features of the relief, scanning electron microscopy was used on a PEM MA 101 instrument.

3. Results and discussion

The structure of MAO coatings was studied on cross sections and on the surface of the samples. MAO coatings have a two-layer structure. A typical structure is shown in Fig. 1. The top layer is technological (its thickness is about 30 % of the total coating thickness). This layer is not wear-resistant, loose, porous, easily removed by sanding with sandpaper. The inner layer is working (basic). This layer is dense with low porosity. Studying the metal-coating interface, it should be noted that there are no delamination, foreign inclusions, discontinuities at the interface. This indicates good adhesion to the AK4 base alloy material.

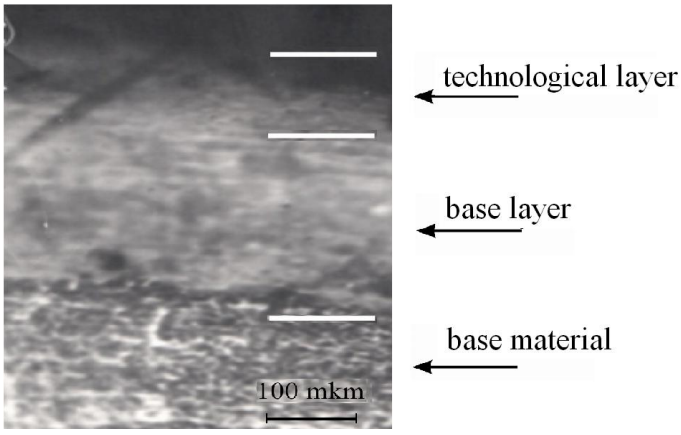


Fig. 1*. Microstructure of the side section of the near-surface layer of the alloy after MAO treatment*

A high roughness of the technological layer and a low one for the base layer of the coating is clearly visible from the data of scanning electron microscopy (Fig. 2).

It was found that the roughness of the base layer is practically not affected by both the composition of the electrolyte (in comparison with the two types that were studied) and the thickness of the coating itself. However, an increase in the current density j from 20 to 30 A/dm^2 in order to accelerate the coating process leads to a significant increase in roughness, which can be seen from Fig. 3.

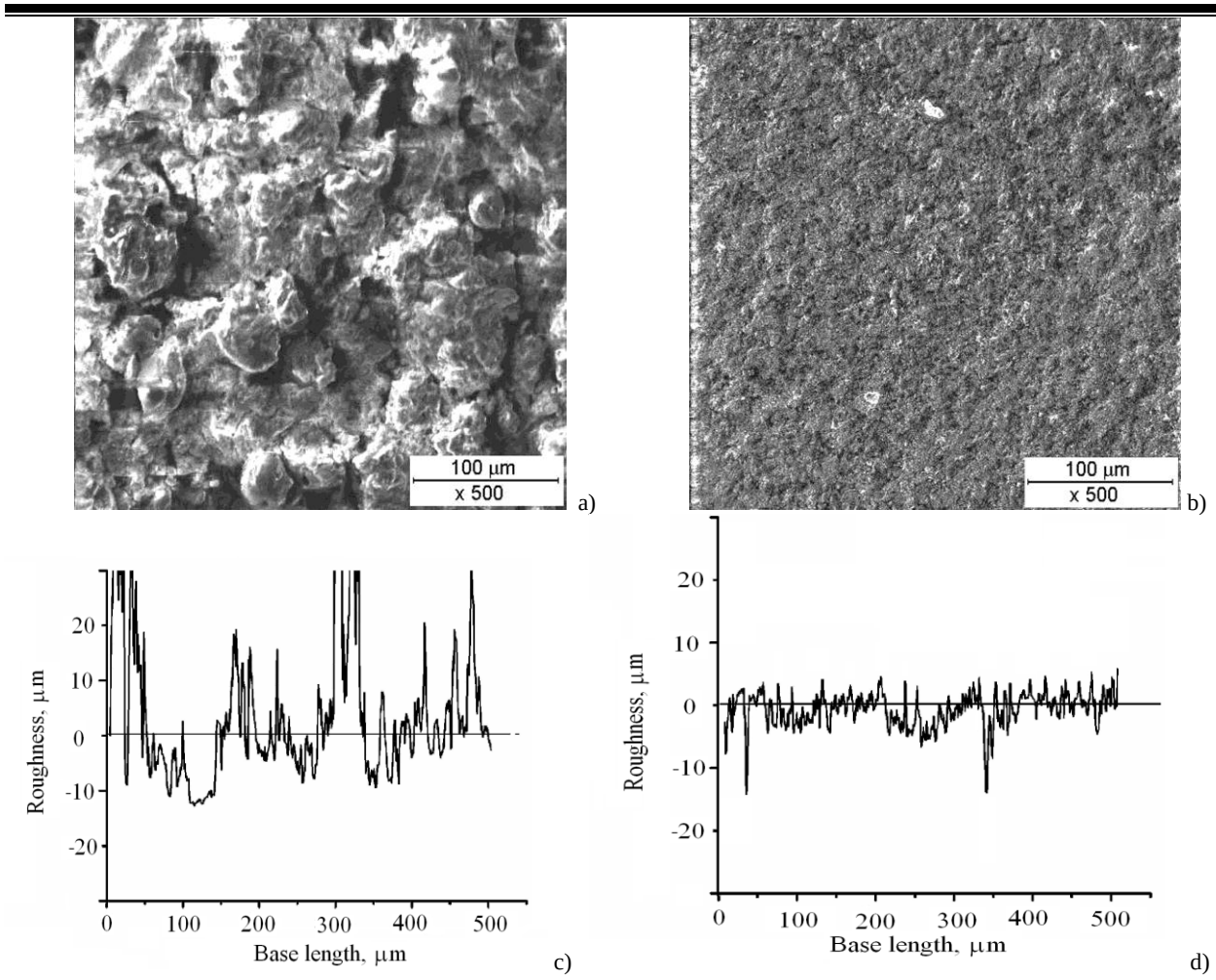


Fig. 2. *SEM images of the surface (a, b) and its roughness (c, d) for the technological layer (a, c) and the base layer (b, d) of the MAO coating on the AK4 alloy*

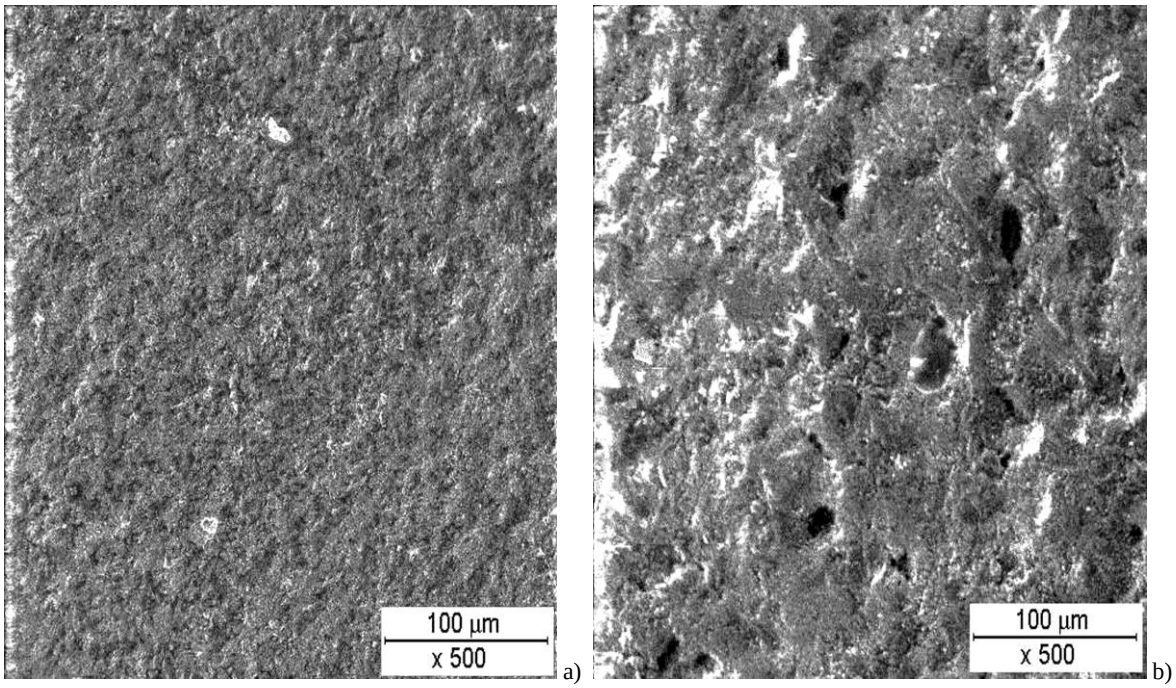


Fig. 3. *The base layer of MAO-coating on the AK4 alloy obtained at a current density of 20 A/dm^2 (a) and 30 A/dm^2 (b).*

The kinetics of coating growth was investigated (Fig. 4). The thickness of the coating was determined by the metallographic method on transverse sections, as well as using a VT-10 NTs vortex thickness gauge. Thus, as the results of determining the thickness of the base layer have shown, at a current density of 20 A/dm^2 and a processing time of 180 minutes, a working wear-resistant layer with a sufficiently large thickness of 150 μm can be obtained.

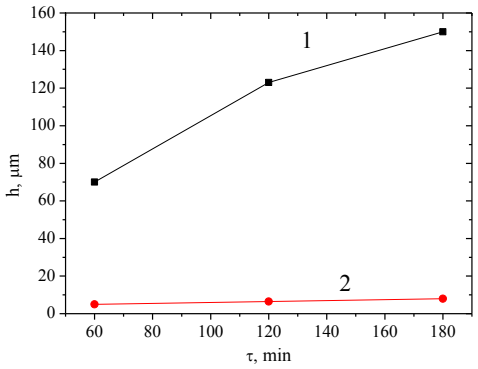


Fig. 4. *Change in the thickness of the base layer from the time of the MAO process (1) and the increase in the thickness of the sample (2)*

Fig. 4 also shows the results of determining the increase in the total thickness of the samples Δt from the time of oxidation. This information about the change in dimensions due to MAO is important since the MAO coating grows both in depth and outside. However, after removal of the technological layer, the change in the sample size is 5 ÷ 10 μm, that is, the coating layer practically does not increase the size of the part after oxidation, which is very important when using such parts in friction pairs.

It should be noted that there should be a change in the size of the samples, since the formed aluminum oxide occupies a larger volume than the initial metallic aluminum. In this case, it should be taken into account that during MAO treatment, not only the transformation of the Al base into oxides occurs, but also the etching of the aluminum base.

The phase composition of the coatings was studied by the X-ray diffraction method. It was found that the coatings consist of crystalline phases. The main phases of MAO coatings are γ- Al_2O_3 and α-Al_2O_3, and the mullite phase $3Al_2O_3{\cdot}2SiO_2$ is also present in a much smaller amount. The results of quantitative phase analysis are shown in table 1.

Table 1. *Quantitative phase composition of MAO coatings and their hardness*

Series number	MAO parameters		Phase composition			
	electrolyte	τ, min	α-Al_2O_3	γ-Al_2O_3	$3Al_2O_3{\cdot}2SiO_2$	HV, MPa
1	2 g/L KOH + 12 g/L Na_2SiO_3	60	1	95	4	14300
2		120	12	74	14	15200
3		180	23	63	14	17100
4	1 g/L KOH + 6 g/L Na_2SiO_3	60	3	88	8	14500
5		120	10	78	12	16500
6		180	16	72	12	17900

Analyzing the results obtained, it can be concluded that the composition of MAO coatings obtained under the same oxidation modes, but in different electrolytes, has a similar phase composition, with the same coating thickness. There is also a tendency to an increase in the relative content of the α-Al_2O_3 phase with an increase in the coating thickness, which may be a consequence of an increase in the breakdown voltage of the dielectric oxide layer. In this case, the temperature in the breakdown channels increases, which creates thermodynamic conditions for the $\gamma{-}Al_2O_3 \rightarrow \alpha{-}Al_2O_3$ transition.

In addition, with an increase in the thickness of the coating, an increase in hardness occurs. As can be seen from table 1, such an increase in hardness correlates with an increase in the relative content of the α-Al_2O_3 phase. With the greatest thickness (about 150 μm), a surface hardness of more than 17000 MPa is achieved. Such a high hardness should ensure higher strength and wear resistance of parts made of AK4 alloy, which is a necessary condition for their use as engine elements.

Thus, taking into account the analysis of the coating hardness, depending on the thickness, it is possible to recommend in practice the use of an electrolyte with a component content in a wide range (KOH within 1 - 2 g/L and Na_2SiO_3 within 6 - 12 g/L), while controlling the thickness of the MAO coating, the required level of hardness can be achieved. This result is very interesting, since it greatly simplifies the MAO technology for parts made of AK4 alloy, namely, it is not necessary to observe the electrolyte composition with great accuracy. It is known that, depending on the electricity passed during the oxidation process, the composition of the bath changes and, as a rule, requires adjustment, but for the process that was developed in this work, this is not necessary.

4. Conclusions

1. The possibility of obtaining wear-resistant coatings on the AK4 alloy by the method of microarc oxidation has been investigated. It was found that in electrolytes with the composition of KOH (1 - 2 g/L) and Na_2SiO_3 (6-12 g/L) at a current density of 20 A/dm^2, an oxide layer with a thickness of about 150 μm and a hardness of 17000 18000 MPa can be formed on the surface.

2. The phase composition of MAO coatings and their hardness were studied. It was found that the main phases are γ-Al_2O_3 and α-Al_2O_3. The quantitative ratio of these phases changes with the thickness of the formed coating. With increasing thickness, there is a tendency for the relative content of the α-Al_2O_3 phase to increase. It is shown that the hardness of the MAO coating depends on the phase composition and increases with an increase in the content of the α-Al_2O_3 phase in the coating.

References

[1] Li H. X., Li W. J., Song R. G., Ji Z. Effects of different current densities on properties of MAO coatings embedded with and without α-Al_2O_3 nanoadditives. Mater. Sci. Technol., 2012, vol. 28, pp. 565-568.

[2] Veys-Renaux D., Rocca E., Henrion G. Micro-arc oxidation of AZ91 Mg alloy: An in-situ electrochemical study. Electrochem. Commun., 2013, vol. 31, pp. 42-45.

[3] He Q., Freakley S.J., Edwards J.K., Carley A.F., Borisevich A.Y., Mineo Y., Haruta M., Hutchings G.J., Kiely C.J. Population and hierarchy of active species in gold iron oxide catalysts for carbon monoxide oxidation. Nat Commun., 2016, vol.7, p. 12905.

[4] Martin J., Leone P., Nomine A., Veys-Renaux D., Henrion G., Belmonte T. Influence of electrolyte ageing on the plasma electrolytic oxidation of aluminium. Surf Coat Technol., 2015. Vol.269, pp. 36–46.
[5] Belozerov V., Mahatilova A., Sobol' O., Subbotina V., Subbotin A. Investigation of the influence of technological conditions of microarc oxidation of magnesium alloys on their structural state and mechanical properties. EasternEuropean Journal of Enterprise Technologies, 2017, vol. 2, n. 5(86), pp. 39-43.
[6] Subbotina V., Al-Qawabeha U.F., Belozerov V., Sobol' O.V., Subbotin A., Tabaza T.A., Al-Qawabah S.M. Determination of influence of electrolyte composition and impurities on the content of α-Al_2O_3 phase in mao-coatings on aluminum, Eastern-European Journal of Enterprise Technologies, 2019, vol. 6, n.12(102), pp. 6-13.
[7] Belozerov V., Sobol' O., Mahatilova A., Subbotina V., Tabaza T. A., Al-Qawabeha U. F., Al-Qawabah S. M. Effect of electrolysis regimes on the structure and properties of coatings on aluminum alloys formed by anode-cathode micro arc oxidation Eastern-European Journal of Enterprise Technologies, 2018, vpl. 1, n.12(91), pp. 43-47.
[8] Klopotov A. A., Abzaev Yu. A., Potekaev A. I., Volokitin O. G. Osnovi rentgenostrukturnogo analiza v materialovedenii. Tomsk: Izd-vo Tom. gos. arhit.-stroit. Un-ta, 2012, 276 p

Layered composites based on niobium with silicide-carbide or silicide-boride hardening

Korzhov Valery Polikarpovich, Kiiko Vyacheslav Mikhailovich, Prokhorov Dmitry Vladimirovich, Zheltyakova Irina Sergeevna
Institute of Solid State Physics, Russian Academy of Sciences, Chernogolovka, Moscow Region

Abstract: *The work is devoted to the development of a solid-phase technology for obtaining high-temperature layered composites from Nb-alloys. The following are presented: one of the options for the formation of the initial multilayer package and its diffusion welding (1), the microstructure of the obtained composites (2) and the results of testing composites (3) for strength at room temperature and temperatures up to 1350°C, taking into account the structure anisotropy, crack resistance and tests for creep with two options for processing the obtained experimental data.*

***KEYWORDS**: COMPOSITE, HEAT RESISTANCE, LAYERED STRUCTURE, NIOBIUM, CREEP, CARBIDE-SILICIDE, CARBIDE-BORIDE, STRENGTH, CRACK RESISTANCE, DIFFUSION WELDING, SOLID PHASE TECHNOLOGY*

1. Introduction

Workings of constructional materials designed for use at high temperatures, based on niobium and molybdenum can result in materials with the highest operating temperature ceiling. The especially high modulus of elasticity for molybdenum and its intermetallic compounds suggests that materials based on it can achieve the highest strength [1–3]. High melting points, strength at high temperatures and creep resistance of niobium and molybdenum compounds, as well as the possibility of organizing increased resistance to oxidation, as, for example, in Mo–Si–B alloys [4], open up a real prospect for obtaining heat-resistant composites based on them.

In addition, the combination of molybdenum or niobium and their purely intermetallic compounds or carbide-silicides in the structure of the composite makes it possible to reduce the density of the composite in comparison with the density of these metals due to the relatively low density of intermetallic compounds and carbide-silicides of niobium and molybdenum [5].

The problem of fracture toughness of composites, which exists in connection with the presence of brittle compounds in their structure, is not insurmountable. One of the possibilities of its solution by decelerating cracks at a weak interface between brittle phases was first shown back in 1964 in [6]. This idea was later used in the development of various layered and fibrous composite materials [7, 8].

In the work, the authors used a "non-melting" method for producing flat products from Nb-alloys, free from the problems of their compatibility with the crucible and guaranteeing the direction of the structure to the product. For its formation, a diffusion method was used, which consists in the solid-phase interaction of two or more components. The directionality of the structure and the interaction of the components were achieved in multilayer stacks of metal foils during their diffusion welding under pressure.

2. Heat-resistant composites from Nb-alloys

2.1. Composites Nb/(Si–C)1 and Nb/(Si–C)2

We investigated layered composites of a multicomponent Nb- alloy with silicide-carbide hardening, obtained by diffusion welding of multilayer packages under pressure in vacuum. The structure of composites was set already at the stage of package assembly.

The elements of the assembly were U-shaped elements made of Nb-foils coated with a multicomponent powder mixture (Fig. 1). The number of items in the package – 15 pcs. Nb foil thickness – 50 microns. One outer and one inner side of the U-elements were coated with a suspension layer of a multicomponent mixture of powders in polyvinyl glycol. Coating composition: 55.2Nb–22.0Ti–8.9Mo–5.6Si–5.4ZrH_2–1.7Cr–1.2 wt. %Al. The zirconium in the powder mixture was in the form of a hydride. Hydrogen was removed from the coating by heating, starting from 350–400°C. The package, made of U-elements, retained its integrity by alternating Nb-foils and coatings. The number of Nb-layers in a package is 30 *pcs.*, The number of coatings is one less.

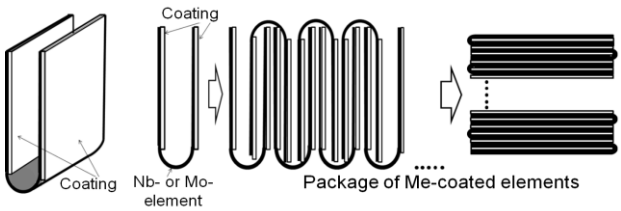


Fig. 1. *Coated element and multilayer bag assembly diagram. On the right is a package made up of U-shaped elements with one inner and one outer cover.*

Diffusion welding of packages Nb/(Si–C)1 and Nb/(Si–C)2 was carried out at 1400°C, but in two modes that differed in welding time and pressure: 1–5 *h* at 8.4 *MPa* and 2 – 10 hours at 15.3 *MPa*. Carbon penetrated into the powder coating while welding the bags from the atmosphere in the welding chamber with a graphite heater.

In fig. 2 shows the microstructures of layered composites Nb/(Si–C)1 and 2. Their thickness after welding is 3.3 and 2.7 *mm*, respectively. Composite thickness with longer welding times was noticeably thinner. The structures are similar in that they consisted of layers inheriting the Nb-foil and layers of the products of sintering powder coatings and their diffusion interaction with the Nb-foil. In the structures of both composites, the layers are designated as (Nb,Ti), indicating that this is an alloy in which the main elements are niobium and titanium. For example, in the Nb/(Si–C)1 (Nb,Ti)-layers the composition was 66.5Nb–24.3Ti–9.2 at. %Me (Me – Mo, Cr, Al and Si) with "traces" of carbon.

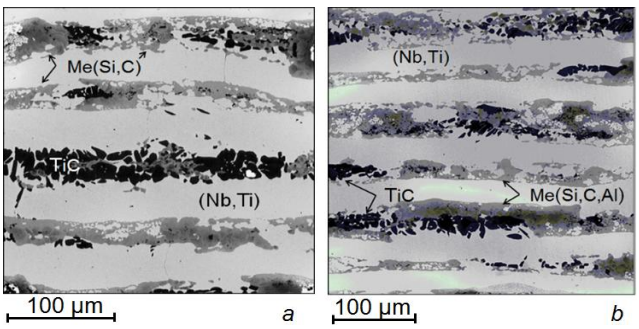


Fig. 2. *Microstructure of composites Nb/(Si–C)1 and 2 after diffusion welding at 1400°C: a – 5 h and 8.4 MPa; b – 10 h and 15.3 MPa*

In composite 2, a change in the concentrations of phase-forming elements, Nb and Ti, in the carbide-silicide phase was traced with distance from the boundary with the (Nb,Ti)-layer. The composition varied from almost equal concentrations of Ti and Nb, ~23.6 at. %, to a concentration ratio in favor of titanium 34.6 at. %Ti and 13.8 at. %Nb → 42.6 at. %Ti and 3,6 at. %Nb:

$$(Ti_{0.47}Nb_{0.47}Me_{0.17})_{1.11}(Si_{0.60}Al_{0.03}C_{0.26})_{0.89} \rightarrow$$
$$\rightarrow (Ti_{0.69}Nb_{0.28}Me_{0.15})_{1.12}(Si_{0.59}Al_{0.02}C_{0.20})_{0.88} \rightarrow$$
$$\rightarrow (Ti_{0.85}Nb_{0.07}Me_{0.24})_{1.16}(Si_{0.61}Al_{0.05}C_{0.17})_{0.84}.$$

The unidentified phase in the composites was a dark gray phase localized within the Me(Si,C) or Me(Si,C,Al) phases. It is not marked in the figures, but according to local X-ray spectral analysis, it is based on Nb, Si, and C: 53.7Nb–0.5Ti–0.2Cr–30.6Si–15.0 at. %C. In terms of concentration, this phase can be assigned to the eutectic regions: (Nb) + α-$(Nb,Me)_5(Si,C)_3$ of the Nb–Si phase diagram or to (Nb) + β-$(Nb,Me)(C, Si)_2$ of Nb–C phase diagrams.

Mechanical characteristics. After DW, the packages had the form of plates, from which specimens were cut in the form of rectangular rods for strength testing by the 3-point bending method at room temperature and high, up to 1350°C, temperatures.

Crack resistance tests were performed on notched specimens. The critical stress intensity factor *K** was calculated under plane deformation conditions using the formula:

$K^* = [P \cdot S \cdot f(a/W)]/B \cdot W^{3/2}$, where *P* is the maximum load, *S* is the base or distance between the supports, *B* and *W* are the width and height of the specimen, and are the depth of the notch. The load was applied from the side opposite to the notch.

Together with the *K** measurements, the effective surface destruction energy *g* of the sample was determined. In theory, strength testing is considered as the separation of a sample into two parts by a macroscopic crack and the formation of two fracture surfaces. Then *g* can be estimated by the ratio of the work of external forces to the doubled area of its cross-section:

$g = (1/2F) \int Q(x)dx$, where *Q* is the load on the sample, *x* is the deflection and *F* is the cross-sectional area of the sample. In reality, this is the area under the experimental load-deflection relationship.

Since the layered structure of the composite has anisotropy, it was useful to apply the load *P* perpendicularly (⊥) and parallel (||) to the layers (*ab*) in the tests for strength and crack resistance for their assessment. In fig. Fig. 3 shows the dependences of the ultimate strength on the testing temperature of the composites Nb/(Si–C) 1 and 2. It was expected that with a load applied parallel to the layers, the strength would be higher. This was the case for the Nb/(Si–C)2 composite (see symbols ○ in Fig. 3, *b*). This is due to the higher moment of resistance of the carbide-silicide layers with a parallel orientation of the direction of application of the load and the plane of the layers. But for the Nb/(Si–C)1 composite with a shorter welding time and pressure at 20°C, this was not observed (see Fig. 3, *a*). Moreover, for P ‖ (ab) σ_B was even less.

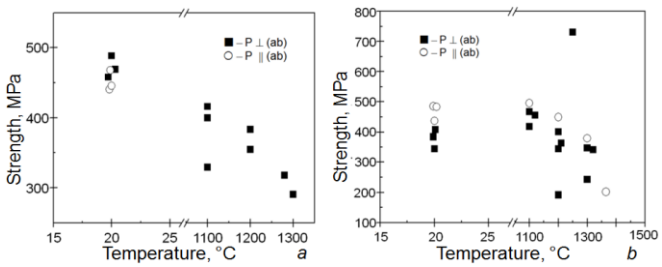


Fig. 3. *Dependences of the ultimate strength σ_B for composites Nb/(Si–C)1 (a) and 2 (b) on the test temperature at P ⊥ (ab) (■) and P ‖ (ab) (○)*

At 20°C, composite 1 had σ_B in the range from 440 to 490 *MPa*, composite 2 – 350–490 *MPa*. However, during temperature tests, the tensile strength of the Nb/(Si–C)1 composite after welding for 5 *h* monotonically decreased, while for the Nb/(Si–C)2 composite after 10 *h* welding σ_B remained at a constant level up to 1200°C. Yes, the strength values had a significant scatter: ~200 *MPa* at 1200°C, but ... there was a measurement at 1250°C with $\sigma_B \approx 750$ *MPa*. According to metallographic analysis data, the crack-resistant structural phase of composite 2 occupied ~66% of the volume. The hardening phases accounted for 15 (carbide) and 16% (intermetallic) volumes. Judging by the experimental data, such a volume of hardening phases is not so small. Probably, the ratio of viscous-plastic and high-strength phases is close to the optimal value, which is reflected in high values of strength at 1100°C and above. For the Nb/(Si–C)1 composite, after diffusion welding for 5 *h*, the crack-resistant component occupied a noticeably larger part of the volume, ~77 vol.%. [The volume amounts of phases were calculated from micrographs (see Fig. 2), in which the TiC, (Nb,Ti) and Me(C,Si)- or Me(C,Si,Al)-phases were colored in different colors].

The results of testing the Nb/(Si–C)2 composite for crack resistance with the calculation of the critical coefficient *K** and the effective surface energy of destruction *g* are summarized in Table. 1. The anisotropy of the structure led to a noticeable difference in the values of fracture toughness *K**, which was 12.8 ± 1.9 when a load was applied perpendicularly and 10.4 ± 1.7 $MPa \cdot m^{1/2}$ – parallel to the layers of the structure.

Table 1. *Results of tests of composites Nb/(Si–C)1 and Nb/(Si–C)2 for crack resistance*

	K*, $МПа \cdot м^{1/2}$	g, $Дж/м^2$		K*, $МПа \cdot м^{1/2}$	g, $Дж/м^2$
P ⊥(ab)	12,0	2690	P ‖(ab)	7,9	2230
	10,8	2120		12,9	2430
	15,6	3280		10,5	1530

The difference in *g* values when a load is applied ⊥-ly and ‖-el to the layers of the structure is explained by the involvement of various types of microfractures in the total fracture and in their number when the macrocrack passes perpendicularly (Fig. 4) or parallel to the layers.

It is of interest to establish a correlation between fracture toughness *K** and effective surface energy *g* (Fig. 5). Based on the still limited data set, it can be stated that the growth of parameters occurs simultaneously.

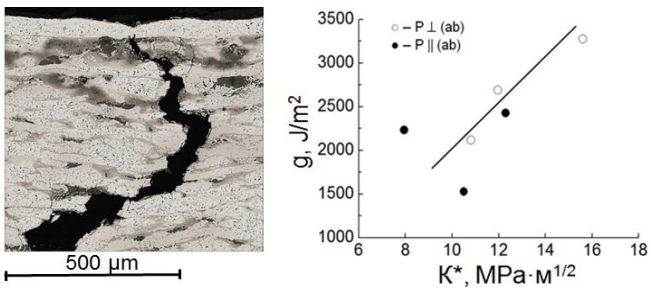


Fig. 4. Trajectory of a macrocrack in the fracture site of the Nb/(Si–C)2 composite at P⊥ (ab)
Fig. 5. Correlation of fracture toughness K with effective surface energy g*

Creep tests. At this stage of the work, for testing samples for creep, the scheme of their 3-point loading was chosen, as one of the most acceptable in terms of requirements for the manufacture of samples (their shape and size). Taking into account the conditions and limitations of this scheme [9], as well as using unconventional methods of processing experimental data [10, 11], it is possible to obtain (as preliminary) results of creep tests for a comparative analysis of the characteristics of developed materials in a relatively short time. Such tests seem to be especially convenient in the conditions of the initial stage of research work.

The high-temperature tests were carried out in the same chamber and according to the scheme as the 3-point bending tests, as well as taking into account the results previously obtained when testing specimens of the same material for short-term strength. The specimen was "stepwise" loaded with specified loads and held at each load under steady-state creep conditions. During the tests, the temperature, load, time and deflection of the sample were recorded. The processing of the results was done proceeding from the power law of creep in tension [12], that is, the behavior of the material in tension was simulated from bending tests: $\dot{\varepsilon} = \eta_n (\sigma/\sigma_n)^n$, where $\dot{\varepsilon}$ is the creep rate, η_n, σ_n and n are constants, one of which must be chosen arbitrarily. Let $\eta_n = 10^{-4}\ h^{-1}$. This means that stress σ_n causes 1% deformation in 100 hours. Following the scheme ([10, 12]) for solving the problem of rod bending under steady-state creep conditions, for our case we obtain an expression that relates the

value of the applied load P [*MPa*] and the deflection rate *v* [*μm/h*] at the center of the rod, i.e. at the place of load application:

(1) $$v = \eta_n \frac{L}{2^{2(n+1)}(n+2)\xi^n(n)} \left(\frac{2P}{\sigma_n bh}\right)^n \left(\frac{2L}{h}\right)^{n+1}$$, where $\xi(n) = \frac{2n}{2n+1}$, *L* is the base length, *b* and *h* are the width and height of the sample. Determining the rate of steady-state creep *v* at various loads from the experimental dependences using expression (1), the values of σ_n and *n* were obtained for the tested samples.

In tests for creep (long-term strength), the sample was loaded with a given load according to the 3-point bending scheme and held there for a given time. The movement of punches was recorded depending on the time. First, there was a choice of clearances in the supports and equipment. When this process ended, the movement of the punch reflected only the deflection of the specimen (Fig. 6, linear sections). The loads were 2, 5 and 6 *kg*. At 2 kg, the sample did not bend for more than 13 hours, which corresponded to the horizontal line of the time dependence of the bending.

The processing of the obtained creep data is as follows.

The exponent n in equation (1) for the deflection rate *v* was determined from the expression

$$v_5/v_6 = (P_5/P_6)_n \text{ , as } n = lg_{(P5/P6)}(v_5/v_6),$$

where P_5 and P_6 are known loads 5 and 6 *kg*, respectively, in the 2nd and 3rd experiments of creep tests, and v_5 and v_6 are the deflection rates calculated similarly to the tangents of the inclination angles of the steady-state creep lines in the 2nd and 3rd experiments, respectively. Indexes 5 and 6 at *v* and *P* repeat loads of 5 and 6 *kg*. Next, we obtain the values of σ_n and n for the tested sample at 1100°C: σ_n = 80.0 *MPa* and n = 3.78. And, finally, we construct the dependence of the creep strain rate έ on the stress σ (Fig. 7).

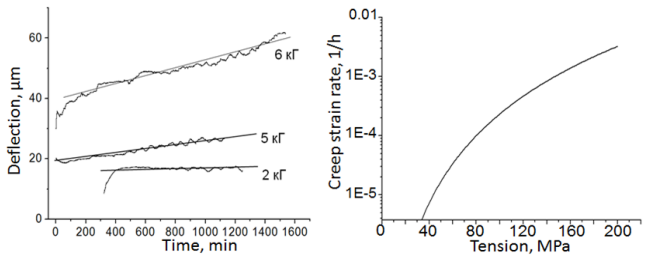


Fig. 6. *Dependence of the deflection in bending on the test time at 1100°C and a load of 2, 5, and 6 kg for the Nb/(Si–C)2 composite*

Fig. 7. *The rate of creep deformation in tension έ depending on the stress σ at v corresponding to 6 kg for the Nb/(S–C)2 composite at 1100°C*

Using the constructed dependence έ = f(σ), we estimate the strength of the obtained composite loaded with a stress of 50 *MPa*. This stress corresponds to the creep strain rate έ, equal to $1.07 \cdot 10^{-5}$ h^{-1}. You can find out how much a rod of length *l* = 100 *mm* will elongate, made of this material in 100 hours: έ = (Δl/l)/ΔT, то

$$\Delta l = \acute{\varepsilon} \cdot \Delta T \cdot l = 1{,}07 \cdot 10^{-5}\ ч^{-1} \cdot 100\ ч \cdot 100\ мм = 0{,}11\ мм.$$

The elongation was 0.11 *mm*.

Conclusions for the section. Microstructure studies show in favor of the chosen method of obtaining heat-resistant composites from multicomponent alloys. Without resorting to melting technologies, layered composites of an alloy of niobium with Ti, Mo, Cr, Zr and Al, strengthened by the compounds of these metals with carbon and silicon, were obtained.

1. The results of strength tests at long exposures and high welding temperatures are aimed at obtaining completed multilayer or layered structures.

2. The values of fracture toughness K* of composites are such that they occupy a position between ceramics and high-strength metal alloys, which is not satisfactory enough. It is possible to improve K* (1) by increasing the proportion of viscous-plastic (Nb)-solid solution in the layered structure of the composite. But it seems more efficient (2) to preserve the viscous-plastic state of the layers inheriting metal alloys in the foil composite.

The point is that Nb foils and alloy foils become stronger as a result of the penetration of carbon, silicon and boron into them during diffusion welding of the packages. To prevent this from happening, it is possible to pre-arrange diffusion barriers against the penetration of C, Si, and B into the visco-plastic layers of the composite, which, possibly, can be thin layers of the same carbides, silicides, and borides.

2.2. Composite Nb/(Si–C)3.

The composite was prepared using a slightly different technique than composites Nb/(Si–C)1 and Nb/(Si–C)2. First, a 2-sided suspension coating of a powder mixture of niobium with Ti, Mo, ZrH_2, Cr, and Al of a certain concentration was applied to the Nb-foils. Coated foils and sections of TRG (thermally expanded graphite) tapes were used to make up a multilayer package, which was heat treated under pressure at a temperature of 1500°C for 2–3 hours. After the package was disassembled (it was easily disassembled), a silicon coating was applied to its surface, and a package was made from such segments, from which, after diffusion welding under pressure, a layered composite in the form of a plate 3–4 mm thick was obtained.

During the second welding, the final sintering (1) of the powder mixture already with silicon and additional penetration of carbon into it, (2) additional alloy formation, (3) diffusion formation of metal carbide-silicides and, in fact, (4) the formation of a layered composite took place. The result of welding in the form of a microstructure of a cross-section at two magnifications and a cross-section of the composite in the fracture zone after a short-term bending test is shown in Fig. 8 and 9.

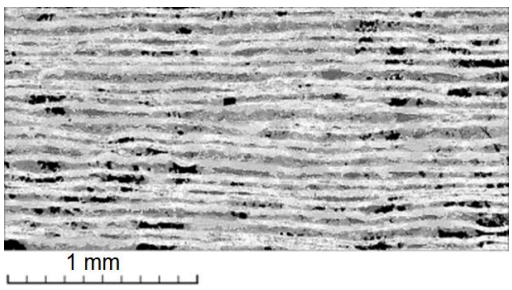


Fig. 8. *Composite Nb/(Si–C)3. Macrostructure of a cross-section after diffusion welding at 1500°C and a pressure of 19 MPa for 3 h*

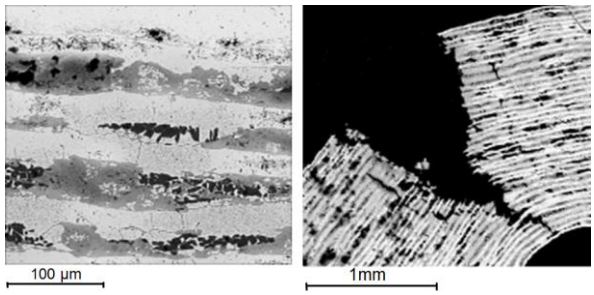


Fig. 9. *Microstructure of the Nb/(Si–C)3 composite after welding and its cross section at the fracture site during 3-point bending tests*

The light layers are identified as Nb-solid solution in place of Nb-foils, between which there are reinforcing layers of metal carbide-silicides.

Creep tests. The composite was subjected to creep tests. The experiments consisted of holding the samples under load at a constant temperature. Temperature range – 1150, 1200, 1250 and 1300°C. The load values were significantly less than the load at which the sample was destroyed during short-term tests. In the experiments, the dependences of the sample deflection on time were obtained. To determine the creep characteristics, the dependence of the creep rate on stress and temperature was used: $\acute{\varepsilon} = K \cdot \sigma_n \cdot e^{Q/kT}$ [equation (1)], where: έ is the creep strain rate, *K* is a constant, σ is the stress, *n* is the rate sensitivity index strain to stress, *Q* is the

activation energy, k is the Boltzmann constant, T is the temperature. The starting points for calculating the parameters of Eq. (1) were the time dependences of the deflection value experimentally measured for each sample at the stage of steady-state creep at three applied stresses and two temperatures. From the data obtained, the deflection rate f was determined.

The relative strain rate $\dot{\varepsilon}$ in the section of steady creep was calculated using the formula for the strain rate (in s^{-1}): $\dot{\varepsilon} = 4h \cdot f/l^2$ (2), where f is the deflection rate (*mm*/s), h is the sample height (mm) and l is the distance between the supports (mm). For further calculations, equation (2) was represented as

$$\dot{\varepsilon}_0 = (s_0/\sigma_0)^n \times (\sigma/s_0)^n \times e^{-Q/kT}, \quad (3)$$

where s_0 = 1 MPa, $\dot{\varepsilon}_0$ (s^{-1}) and σ_0 (MPa) are constants. At constant temperature, expression (3) was represented as: $\dot{\varepsilon} = N \times (\sigma/s_0)^n$ (4), where $N = \dot{\varepsilon}_0 \cdot (s_0/\sigma_0)^n \cdot e^{-Q/kT}$ [equation (5)].

The parameters N and n are determined from the graph $\dot{\varepsilon} = f(\sigma)$, presented in logarithmic coordinates, at each test temperature.

The constants $M = \dot{\varepsilon}_0 \times (s_0/\sigma_0)^n$ and Q were determined from two equations (5) for two different temperatures (Fig. 10).

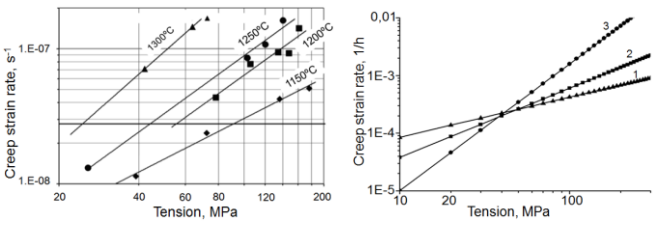


Fig. 10. *Dependences of the creep rate on stress for the Nb/(Si–C)3 composite at temperatures in the range 1150–1300°C.*
Horizontal line drawn at 100-hour strength

Fig. 11. *Dependences of the creep strain rate $\dot{\varepsilon}$ on stress for the composite Nb/(Si–C)3: 1 – 50 MPa, 1150°C; 2 – 52.55 MPa, 1150°C; 3 – 45.28 MPa, 1300°C*

Evaluation of the dependence of the creep strain rate of the composite at different temperatures shows that the 100-hour creep limit (horizontal line in the figure) of the Nb/(Si–C)3 composite decreases with an increase in the test temperature from 90 *MPa* at 1150°C to 25 *MPa* at 1300°C (Fig. 10).

The results obtained were compared with similar results for cast (Nb–Si)-alloys obtained by directional solidification. Such studies with the processing of experimental data using a similar technique were carried out in our laboratory. The comparison showed that the Nb/(Si–C)3 composite had a higher level of 100-hour strength than the (Nb–Si)-alloys with a directed structure at 1150°C: 90 and 60 *MPa*, respectively.

Creep tests, but with processing already according to the method known here, which we used for the Nb/(Si–C)2 composite [10–12]. The method simulates flexural testing as the tensile behavior of a material. Using the constructed dependences for $\dot{\varepsilon} = f(\sigma)$, we now estimate the strength of a composite based on a multicomponent Nb-alloy loaded with a stress of 50 *MPa* (Fig. 11). This stress in these experiments at 1150°C corresponds to the creep strain rate $\dot{\varepsilon}$, equal to $0.98 \cdot 10^{-5}$ h^{-1}. Then a rod with a length of l = 100 *mm*, made of such a material, will lengthen by 98 μm in 100 hours: $\dot{\varepsilon} = (\Delta l/l)/\Delta T$, then

$\Delta l = \dot{\varepsilon} \cdot \Delta T \cdot l = 0.98 \cdot 10^{-5}$ $h^{-1} \cdot 100$ $h \cdot 100$ *mm* = 0.098 *mm*.

Note that, in contrast to Fig. 7, here the dependences $\dot{\varepsilon} = f(\sigma)$ are given in logarithmic scales along both axes.

2.3. Composite Nb/(Si–B)

The anisotropy of the layered structure in the composite caused anisotropy of the strength properties in bending tests if a load was applied perpendicularly and parallel to the plane of the layers. The dependence of strength on the test temperature for this composite is shown in Fig. 12. Anisotropy persists at temperatures of 1100–1300°C.

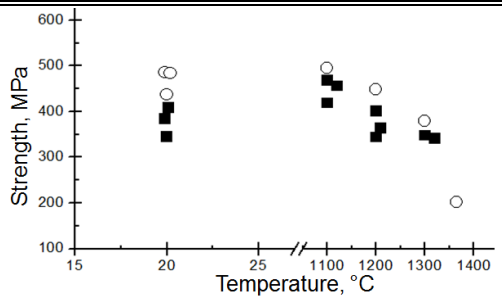


Fig. 12. *Dependence of $\sigma_{B\perp}$ (●) and $\sigma_{B||}$ (○) composite Nb/(Si–B) with unpolished surfaces on the test temperature*

The lower strength at room temperature than at 1100°C in the composite was due to the roughness of the two surfaces of the test pieces after spark cutting. For the same composite with surfaces polished after spark cutting, the strengths in the perpendicular and parallel directions at room temperature were equal: $\sigma_{B\perp}$ = (600 ± ± 180) and $\sigma_{B||}$ = (790 ± 48) *MPa*. Anisotropy $\sigma_{B||}/\sigma_{B\perp}$ = 1.32. In high-temperature tests, the quality of the sample surfaces did not affect the strength of the composite. The average strength level of the composite reinforced with silicon and boron compounds was ~450 *MPa* at 1100°C and ~350 *MPa* at 1300°C.

This work was financially supported by the Russian Foundation for Basic Research (project No. 20-03-00296).

REFERENCES

1. Properties, production and application of refractory compounds. Ed. T. Ya. Kosolapov. M.: Metallurgy, 1986, - 928 p.

2. Schneibel J.H. *High temperature strength of Mo–Mo_3Si–Mo_5SiB_2 molybdenum silicides.* Intermetallics, 2003, No 11, pp. 625–632.

3. Sharif A.A., A. Misra, T.E. Mitchell *Strength of $MoSi_2$-based crystals at ultra-high temperature.* Scripta Materialia, 2005, No 52, pp. 399–402.

4. Jain P., K.S. Kumaru *Tensile creep of Mo–Si–B alloys.* Acta Materialia, 2010, v. 58, No 6, pp. 2124–2142.

5. Goronovskii I.T., Yu.P. Nazarenko, E.F. Nekryatch. A short guide to chemistry. Kiev: Naukova dumka, 1987, – 929 c.

6. Cook J., J.E. Gordon. Proceedings of the Royal Society, 1964, v. 282, No 8, pp. 508.

7. Anischenkov V.M., S.T. Mileiko. DAN USSR, 1978, v. 241, No 5, p. 1068.

8. Mileiko S.T. *Oxide-fibre/Ni-based matrix composites – III: A creep model and analysis of experimental data.* Composite Science and Technology, 2001, v. 61, pp.1649–1652.

9. Ruditsin M.N., P.Ya. Artemov, M.I. Lyuboshits. Reference book on the strength of materials. Minsk: Higher school, 1970. – 628 c.

10. *Mileiko S.T. Oxide-fibre/Ni-based matrix composites – III: a creep model and analysis of experimental data*. Composites Science and Technology, 2002, v. 62, pp. 195–204.

11. *Mileiko S.T., V.M. Kiiko. High-temperature creep of fiber composites with a metal matrix at alternating stresses.* Mechanics of Composite Materials, 2004, v. 40, p. 523–534.

12. Ju. N. Rabotnov. Mechanics of a deformable solid. Moscow: Nauka, 1979. –744 p.

13. Karpov M.I., V.I. Vnukov, T.S. Stroganjva et al. Influence of silicon content on microstructure and mechanical properties of an alloy based on the niobium-silicon system. Izvestia RAN. Physical series. 2019, v. 83, No 10, p. 1353–1361.

14. Svetlov I.S., M.I. Karpov, T.S. Stroganjva, D.V. Zaitsev, Yu.V. Artemenko. High-temperature in-situ creep of composites of the Nb-Si system. Deformation and destruction of materials, 2019, No 11, p. 2–6.

Hydrophilized unsaturated polyester resin based on a two-component system of sulfur and cement

Assoc. Prof. Cherkezova R. PhD., Ch.Assist. Prof. Hristova T. PhD, Assist. Prof. Zafirova K.
Medical University „Prof. Dr. Paraskev Stoyanov"- Varna,Bulgaria;
E-mail: rumchara@abv.bg, Tatiana. Hristova@mu-varna.bg , Kristina.Zafirova@mu-varna.bg

Abstract: *This work develops a multicomponent system comprising unsaturated polyester resin (UPER) hydrophilizing a two-component system of sulfate-resistant cement (SC) and sulfur, diluent water and a redox system. The hydrophilized unsaturated polyester resin (HUPER) so obtained can be used as a basis for polymer-silicate composites with good strength properties, precise embossed printing on the surface of various molds, and good visual characteristics. Polymer-silicate compositions with low and high content of SC were selected, and the constant amount of SC in the two groups obtained corresponded to a gradual change in sulfur content. Time kinetic dependencies of the cross-linking process of unsaturated polyester at a given amount of redox system were monitored. Reproducibility of results for different polymer compositions was achieved thereby enabling a possibility to predict them.*
KEYWORDS: *HYDROPHILIZATION, RESIN/MINERAL DISPERSE SYSTEM, CEMENT, SULFUR.*

1. Introduction

This work is a continuation of the development of various methods for hydrophilization of UPER, which is a component of a multicomponent polymer system. In this specific case, we use SC and sulfur (S) as hydrophilizers in different proportions. A literature review shows that there are studies on UPER including the invidivual influence of SC[1-3]; just a few studies of the effects of sulfur are found [4,5]. A matter of interest is the influence of the two components, which may be confined to the quantitative proportion thereof. Cross-linking by a redox system of cobalt naphthenate (CN) and cyclohexanone peroxide (CHP) of UPER is not inhibited by the presence of the two hydrophilizing components, and what is more, it is also possible when the system is diluted with water [5-7].

The samples obtained based on different compositions are technologically reproducible which is proven by a large number of experiments with averaged results. The results of studies on the hardening kinetics and strength properties allow us to forecast the characteristics of resulted materials.

2. Materials and methods

2.1. Materials

We used:

Resin of type Vinalkyd 550 PE-R (Orgachim Resins – Ruse) containing 35% styrene and 65% unsaturated polyesters, which is a condensation product of propylene glycol and maleic anhydride. A 50% solution of cyclohexanone perodxide in dibutylphthalate was used as a curing initiator, and a 10% solution of cobalt naphthenate in styrene was the accelerator.

Sulfate-resistant blast furnace cement CEM III A-S 42.5 N SR – Devnya Cement, town of Devnya (SC).

Sulfur powder (S), A.R. (purum p.a. ≥99%) – Sigma – Aldrich.

2.2. Methods

Methods of obtaining compositions based on unsaturated polyester resin hydrophilized with cement have been developed, in which the percentage of water is always 50% in relation to cement, sulfur is in different amounts in relation to cement, and a CN/CHP redox system in constant proportion in relation to resin.

Test pieces were examined for impact strength according to Izod by Izod impact testing machine GB1843-2008.

Test pieces were examined for compression strength by means of HZ-1005 Computer-type Tensile Testing Machine. Flexural stress and flexural modulus are calculated according to EN ISO 178:2019.

3. Results and discussion

The mass of all components included in the development of HUPER was summed up and reduced to 100%. A minimum amount of SC (12.8%) was used in the particular multicomponent polymer system whose data are provided in Table 1. Table 1 presents data on different compositions according to the technology for the amount of added water, which should be 50% in relation to the quantity of SC.

Table 1*. Data on the obtaining of compositions based on UPER hydrophilized with different amounts of sulfur at constant quantity of SC (12.8% ± 0.02%), and 50% of water in relation to the quantity of SC.*

Composition No.	S quantity %	Time [τ, min]	Temperature T max, ˚C]
1	0	29	95,5
2	0,03	32	124
3	0,05	52	110
4	0,08	49	85,5
5	0,1	71	64,5
6	0,13	11	41

The development of that system resulted in experimental material of a large number of samples, five of which were selected, including a reference standard at 0% S. The composition of those samples include various gradually changing amounts of sulfur and allows the kinetics of the polymerization process to be traced (Fig.1).

There are 6 kinetic curves corresponding to the samples selected. Each kinetic dependency was obtained by reading the temperature change associated with to the release of a specific amount of heat at regular intervals (1 minute) reaching experimentally to a given temperature peak. The temperature so reached corresponds to gelation, which is consistent to a certain degree with HUPER cross-linking. It is observed that the peak temperature depends on the amount of sulfur. Curves 2 and 3 in which the amount of sulfur is 0.03% and 0.05%, respectively, indicate a sharp increase in the peak temperature versus the standard process at 0% S (curve 1). However, the greatest increase in the amount of sulfur from 0.05% to 0.08% results in a sharp increase in the gelation time when the temperature peak drops, which is most pronounced for sample 6 (curve 6): the temperature is 2.5 times lower.

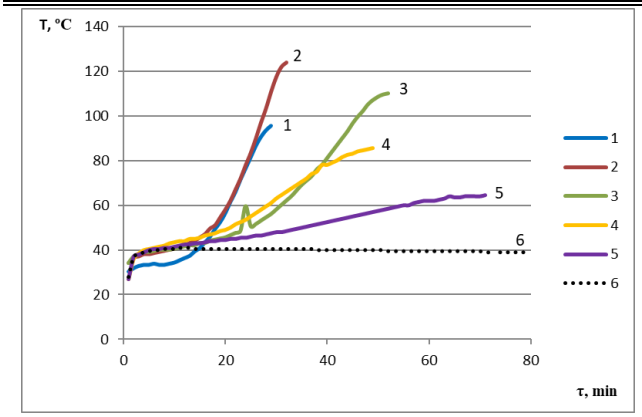


Fig. 1. *Kinetics of the polymerization process, where curve 1- 0% S, curve 2 – 0.03% S, curve 3 – 0.05% S, curve 4- 0.08% S, curve 5 – 0.1% S, curve 6 – 0.13% S (according to Table 1)*

Two groups of kinetic dependencies are therefore formed:
The first group (from 0.03% to 0.05% S) is characterized by gradual increase in the gelation time, as the temperature is still above the standard; The second group (from 0.08% to 0.13% S), which is characterized by significant increase of time with gradual decrease in the peak temperature.
It follows that the characteristics of samples examined could be forecasted in reference with their future use for technological purposes.
The data in Table 2 were obtained from similar development of multicomponent hydrophilized polymer system (100%), as in this case the amount of SC used is 36.2%. The requirements for the amount of water are technological (50% in relation to SC).
In this situation, 5 samples were also taken and compared against the reference (zero sample), where the amount of sulfur is different at the same quantity of SC.

Table 2. *Data on the obtaining of compositions based on UPER hydrophilized with variable amounts of sulfur at constant quantity of SC (36.2% ± 0.02%) and 50% of water in relation to the quantity of SC.*

Composition No.	S quantity %	Time [τ, min]	Temperature T max, ˚C]
1	0	27	46
2	0,01	47	67,5
3	0,03	58	56
4	0,04	50	45,5
5	0,06	21	37
6	0,07	10	37,5

The idea of so selected hydrophilzing components (SC and S) forming a two-component hydrophilizing system (Table 1 and Table 2) is first to monitor the influence of sulfur at constant amount of SC, and second, to record the influence of SC at equal masses of sulfur.
Fig. 2 presents kinetic curves T,˚C /τ,min for samples at the indicated quantity of SC and gradual increase in the amount of sulfur, as the kinetic dependency of the zero sample is used for comparison. In this cas, it is obvious that the peak temperature and the time to reach it are also influenced by the change in the amount of sulfur, however the nature of curves differs from that in Fig. 1, which is due to the larger quantity of SC. At smaller amounts of sulfur (curves 2 and 3), temperatures are also higher than the temperature of the reference sample but are twice lower than the corresponding curves at lower quantity of SC. Curves 4 and 5 in Fig. 2 (compared to the zero sample) have lower peak temperatures, as the gelation time in this case is considerably higher (hours and days) compared to the kinetic dependencies presented in Fig. 1.

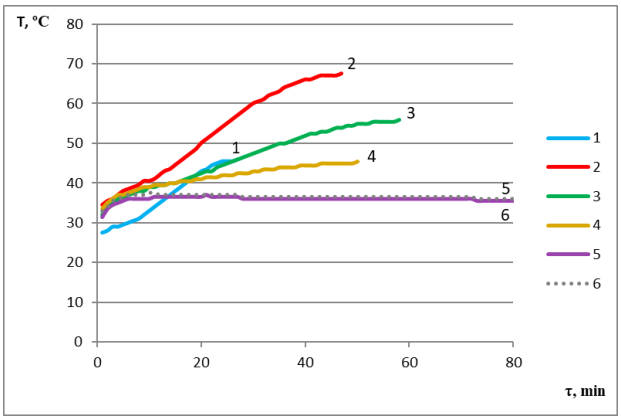


Fig. 2. *Kinetics of the polymerization process, where curve 1- 0% S, curve 2 – 0.01% S, curve 3 – 0.03% S, curve 4 – 0.04% S, curve 5 – 0.06% S, curve 6 – 0.07% S (according to Table 2)*

It follows that the quantity of SC is of utmost importance. For example, it is obvious for curves 2 in Fig. 1 and Fig. 2, in which the amount of sulfur is the same and the quantity of SC is three times different, that the peak temperature is twice higher at smaller quantity of SC, and is reached in a significantly shorter period (32 min. relative to 47 min.).
Namely these results enable the variartion of quantitative compositions in order to be used in the technological development of a material with pre-set curing time. This is the meaning of the forecast characteristics of materials and the possibility for their reproducibility in accordance with formulants.
Strength tests were carried out on so selected samples from 1 to 6. Results of impact strength, flexural strength and elasticity modulus are presented below.
The data in Fig. 3 suggests that, at 12.8% SC, the values of that strength indicator are higher at larger amouns of sulfur (0.05% and 0.08%) and lower at 0.1% and 0.13%. It follows from the same figure that a larger quantity of SC does not influence the values, excluding the sample with the highest content of sulfur.

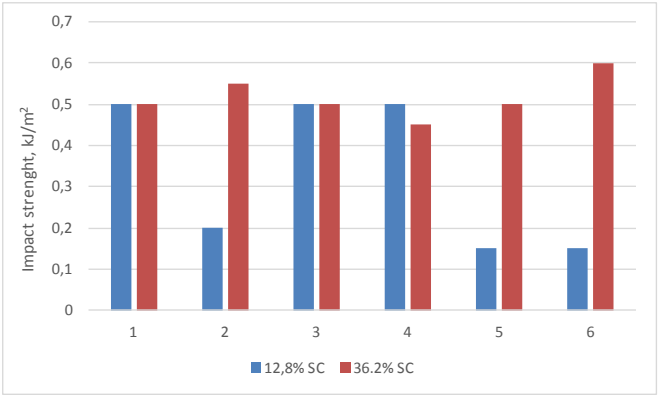


Fig. 3. *Impact strength data in polyer compositions at constant composition of SC (12.8% and 36.2%) and gradual change in the amount of sulfur (according to Table 1 and Table 2)*

The flexural strength data (Fig. 4) suggests that this indicator lowers its value as compared to that of the reference sample. The

interesting thing here is the amount of sulfur 0.13% which has a different influence – the value is the lowest at the lowest amount of sulfur, and the highest at the high amount of sulfur.

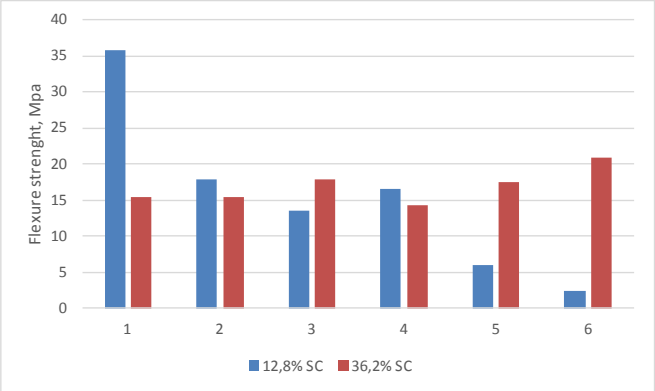


Fig. 4. *Flexure strength data in polymer compositions at constant quantity of SC (12.8% and 36.2%) and gradual change in the amount of sulfur (according to Table 1 and Table 2)*

The elasticity modulus (Fig. 5) presents a peculuar peak at 0.05% amount of sulfur, the same peak is shifted to the highest quantity of SC (36.2%) and the highest amount of sulfur (0.07%).

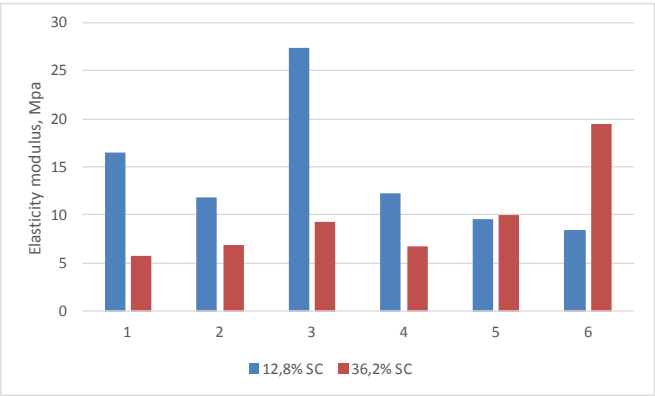


Fig. 5. *Elasticity modulus data in polymer compositions at constant quanitity of SC (12.8% and 36.2%) and gradual change in the amount of sulfur (according to Table 1 and Table 2)*

4. Conclusion

The development of a multicomponent polymer system and the selection of different compositions based on it enable us to make various surveys resulting in the following more significant conclusions:

1) Kinetic dependencies at two different quantities of SC with gradially changing amount of sulfur were traced, and it was established that the gelation time was more influenced at lower quantity of SC (12.8%), i.e. kinetic curves have more proncounced extreme nature.
2) Subject to compliance with the formulation data when preparing the compositions of different samples, a comparative characteristics of the peak temperature and the curing time could be made and reproducibility of results and projected characteristics of materials could be achieved.
3) The impact strength data suggested that the values of that indicator were largely insensitive to changes in the amount of sulfur at 36.2% SC. At 12.8% SC, there is a dependency on the amount of sulfur, which will be the subject of future studies.
4) The flexure strength data suggested that the values of that indicator were the highest at 12.8% SC and 0.05% S. Such peak in the value of the indicator occured at 36.2% SC and 0.07% S.

The shift in the peak at different quantities of SC and sulfur will also be a subject of other scientific research.

5. References

1. Fowler, D. W. Polymers in concrete: a vision for the 21st century. *Cement and Concrete Composite*.1999, 21(5-6), 449-52.
2. Vipulanandian, C., E. Paul. Performance of Epoxy and Polyester Polymer Concrete. *ACI Materials Journal*. 1990,87(3),241-51.
3. Maksimov, R.D, L. Jirgens, J. Jansons, E. Plume. Mechanical properties of polyester polymer-concrete. *Mechanics of Composite Materials*. 1999, 35, 99–110.
4. Reda Taha, M., M.Genedy, Y.Ohama. Developments in the Formulation and Reinforcement of Concrete (Second Edition). 17 - Polymer concrete.*Woodhead Publishing Series in Civil and Structural Engineering*.2019, 391-408.
5. Cherkezova, R. Patent №63168 (Bulgaria), applied 1997, issued 2001.
6. Paturoev, V. V. , Polymer concrete technology. *Stroiizdat*, Moscow. 1976, 159.
7. Simeonov, I. , Yu Hristova. Polymer concrete. *Bulgarian Acad. Sci.*, Sofia. 1980, 250.